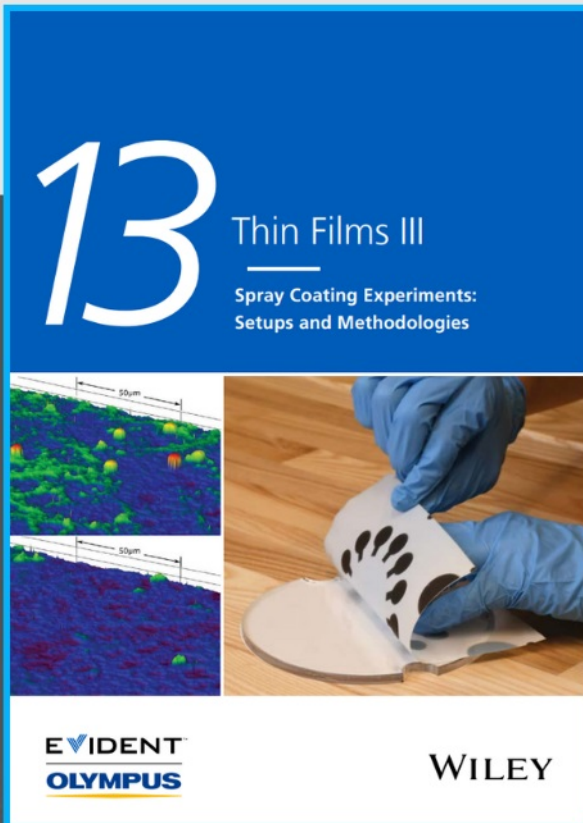




# Spray Coating Experiments: Setups and Methodologies



**The latest eBook from  
Advanced Optical Metrology.  
Download for free.**

*Spray Coating Experiments: Setups and Methodologies*, is the third in our Thin Films eBook series. This publication provides an introduction to spray coating, three article digests from Wiley Online Library and the latest news about Evident's Image of the Year Award 2022.

Wiley in collaboration with Evident, are committed to bridging the gap between fundamental research and industrial applications in the field of optical metrology. We strive to do this by collecting and organizing existing information, making it more accessible and useful for researchers and practitioners alike.

**EVIDENT**  
**OLYMPUS**

**WILEY**

# A Review of X-Ray Imaging at the BAMline (BESSY II)

Henning Markötter,\* Bernd Randolph Müller,\* Andreas Kupsch, Sergei Evsevlev, Tobias Arlt, Alexander Ulbricht, Shahabeddin Dayani, and Giovanni Bruno

The hard X-ray beamline BAMline at BESSY II (Berlin, Germany) has now been in service for 20 years. Several improvements have been implemented in this time, and this review provides an overview of the imaging methods available at the BAMline. Besides classic full-field synchrotron X-ray computed tomography (SXCT), also absorption edge CT, synchrotron X-ray refraction radiography (SXRR), and synchrotron X-ray refraction tomography (SXRCT) are used for imaging. Moreover, virtually any of those techniques are currently coupled in situ or operando with ancillary equipment such as load rigs, furnaces, or potentiostats. Each of the available techniques is explained and both the current and the potential usage are described with corresponding examples. The potential use is manifold, the examples cover organic materials, composite materials, energy-related materials, biological samples, and materials related to additive manufacturing. The article includes published examples as well as some unpublished applications.

of X-ray fluorescence spectroscopy (XRF) and X-ray absorption spectroscopy (XAS),<sup>[2]</sup> also imaging by means of X-ray tomography (XCT) and radiography, based on absorption, phase, and refraction contrast, is performed.<sup>[3]</sup> These nondestructive methods are exploited for the characterization of structures and defects at the micrometer scale and below. While large metal-based components for example are usually tested with laboratory-based XCT scanners, miniaturized components smaller than a centimeter are well studied with synchrotron imaging (for instance additively manufactured metal samples). This holds a fortiori for small components made of light materials, including metallic alloys, polymers, and carbon fiber-reinforced polymers. Additionally, the imaging methods imple-

mented at the BAMline are also available to the large scientific community, that is, users from around the world; this covers many more scientific areas that are granted with beamtime. All user experiments are then formally handled by HZB and supported scientifically by BAM staff. In this article, we point out the imaging possibilities that are available at BAMline, each with a short description, important works in different fields, and corresponding examples.

## 1. Introduction

The BAMline was the first beamline with a 7T wavelength shifter (WLS) for hard X-rays installed in 2000 at Berlin Electron Storage Ring for Synchrotron Radiation (BESSY II).<sup>[1]</sup> It was developed and installed by the Bundesanstalt für Materialforschung und -prüfung (BAM) and the Physikalisch-Technische Bundesanstalt (PTB). At present, the BAMline is operated and supervised by the BAM; available beamtime is shared between BAM (50%), PTB (25%), and external users (25%), who can apply for it via the beamtime proposal system GATE of the Helmholtz-Zentrum Berlin (HZB, which operates BESSY II). The beamline is used for nondestructive material characterization by means of spectroscopic as well as imaging methods. Besides different types

## 2. Synchrotron X-Ray Computed Tomography (SXCT)


X-ray and especially synchrotron X-ray computed tomography (SXCT) are well-established methods for nondestructive testing and characterization in a large variety of research fields. It is based on the attenuation of X-rays through a sample. A set of projection images (radiographs) from different angles are collected and used to reconstruct the 3D structure. **Figure 1** shows the experimental setup at the BAMline.

A double-multilayer monochromator (DMM) of the BAMline delivers monochromatic X-rays for the SXCTs.<sup>[4]</sup> With the monochromatic beam the attenuation follows the Lambert–Beer law (exponential) and a suited reconstruction software computes the 3D distribution of attenuation coefficients within the sample. One of the most important advantages of SXCT with respect to laboratory XCT is the absence of the so-called “beam hardening” artefacts, which occur if one uses a polychromatic X-ray beam. The attenuation coefficient depends on the material and on the beam energy. The high flux at a synchrotron beamline allows using a monochromator while still delivering enough photons to conduct experiments in a reasonable amount of time.

H. Markötter, B. R. Müller, A. Kupsch, S. Evsevlev, A. Ulbricht, S. Dayani, G. Bruno

Department of Non-Destructive Testing  
Abteilung Zerstörungsfreie Prüfung  
Bundesanstalt für Materialforschung und -Prüfung (BAM)  
Unter den Eichen 87, 12205 Berlin, Germany  
E-mail: henning.markoetter@bam.de; bernd.mueller@bam.de

T. Arlt  
Helmholtz-Zentrum Berlin  
Hahn-Meitner-Platz 1, 14109 Berlin, Germany

 The ORCID identification number(s) for the author(s) of this article can be found under <https://doi.org/10.1002/adem.202201034>.

© 2023 The Authors. Advanced Engineering Materials published by Wiley-VCH GmbH. This is an open access article under the terms of the Creative Commons Attribution License, which permits use, distribution and reproduction in any medium, provided the original work is properly cited.

DOI: 10.1002/adem.202201034

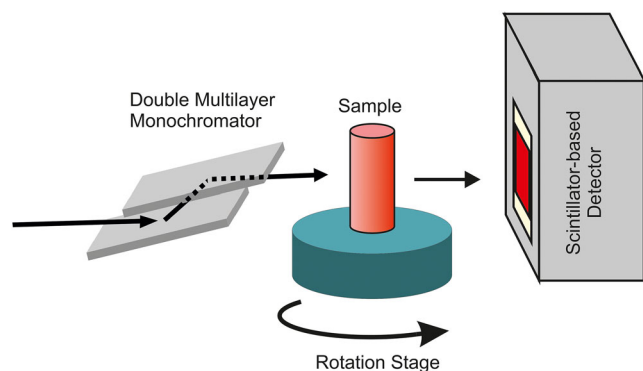


**Figure 1.** Experimental setup at the BAMline for computed tomography (SXCT). Synchrotron X-rays are monochromatized with a DMM. The sample is rotated in the beam along an axis perpendicular to the beam direction while projection images are acquired in a 2D detector.

The monochromaticity of the X-ray beam allows precise determination of the beam attenuation according to Lambert–Beer’s law. A monochromatic beam does not cause the so-called beam hardening effect, which is unavoidable if a continuous spectrum is used, as in laboratory equipment (for details see the study by Buzug et al.).<sup>[5]</sup>

In general, lower energies result in stronger attenuation and a higher contrast is achieved, whereas higher energies allow a higher transmittance through the samples. Another great advantage of SXCT with a monochromator is that the beam energy can be adapted to the density and thickness of the samples.

The main drawback of SXCT is the eternal compromise between spatial resolution and field of view (FoV). There are only “patches” to this problem and cunning solutions on a case-by-case basis. Other challenges concern the speed of acquisition (relevant for real-time studies) and the use of

ancillary techniques or in situ equipment (relevant for materials performance).

The main components of an XCT setup are the sample manipulation and the detector systems. The sample manipulation system allows rotating the sample around the vertical axis and translating it via motorized stages. Additional stages allow aligning the rotation axis and the sample to optimize results. The detector system uses a scintillating screen to convert X-rays into visible light. The converted image is focused with lenses via a mirror onto the chip of a charged coupled device (CCD) or a scientific Complementary metal-oxide-semiconductor (sCMOS) camera (Figure 2). The collected projections are used for a volumetric reconstruction. This can be conducted for example by a filtered back projection in the 3D space.<sup>[6]</sup> Other reconstruction algorithms are currently available for special cases, where for instance a limited number of projections is available or circular sectors cannot be accessed during the sample rotation (see other studies).<sup>[7,8]</sup> This last subject is vast and goes beyond the scope of this work.

Over the two decades since BAMline was established, the imaging setups have been repeatedly modified and further developed. In particular, the absorption imaging detector has undergone a major upgrade in 2021.<sup>[9]</sup> The current parameters of this detector will be mentioned here with the note that many of the examples shown were realized with previous setups. However, the measurement principle itself has not changed, mostly pixel sizes and exposure times have changed over time.

SXCT can be performed using a DMM with W/Si layers in monochromatic mode ( $\approx 3.5\%$   $dE/E$ , typically between 8 and 60 keV, a flux of  $8.0 \times 10^{10} \text{ s}^{-1} \text{ mm}^{-2}$  @20 keV, and  $4.0 \times 10^{10} \text{ s}^{-1} \text{ mm}^{-2}$  @40 keV) or with a single Pd layer in pink beam mode. It can be chosen to do “step scans” in which the rotation stage stops for each exposure or “on-the-fly” scans in which the motor continuously rotates during the exposures.

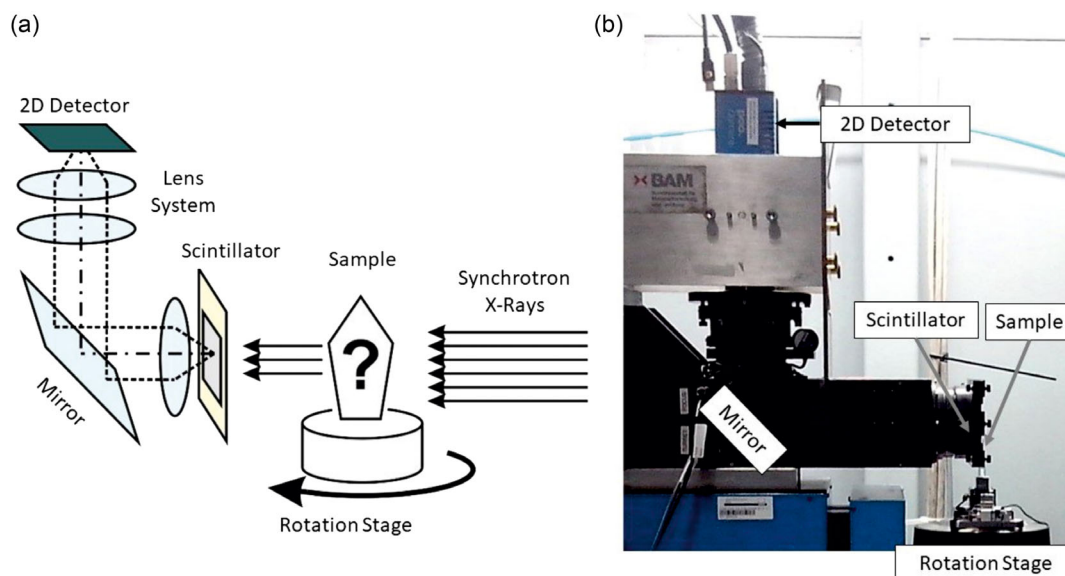


**Figure 2.** a) The basic principle of synchrotron imaging shown in a sketch and b) a photograph at the BAMline. The synchrotron X-ray beam transmits a sample, and its projection is converted by a scintillator screen into visible light, which is recorded by a camera. For tomography, the sample is rotated by a rotation stage.

**Table 1.** Available FoVs and resolutions for the SXCT setup in combination with a sCMOS camera (PCO.edge 5.5 with a resolution of  $2560 \times 2160$  pixel).

Lens	FoV	Pixel size
2×	$9.2 \times 7.8 \text{ mm}^2$	$3.6 \mu\text{m}$
5×	$3.7 \times 3.1 \text{ mm}^2$	$1.44 \mu\text{m}$
10×	$1.8 \times 1.5 \text{ mm}^2$	$0.72 \mu\text{m}$
20×	$0.92 \times 0.78 \text{ mm}^2$	$0.36 \mu\text{m}$

This results in a much faster acquisition and the scan times reduce from roughly 1–2 h down to 15–30 min.

For the detector, a set of four lenses and thus FoVs can be chosen to adapt to different sized samples (Table 1). Along with a sCMOS camera (PCO.edge 5.5), CdWO<sub>4</sub> scintillators are paired with the X-ray microscope.

The rotation stage (Micos UPR160A) is equipped with a XY piezostage for sample positioning as well as an electric slip ring feeding 8 channels (up to 1 A each) through the stage onto the rotating top. Alternatively, a Huber 410 rotation stage is available for loads larger than 0.5 kg. Furthermore, there is additional equipment which can be used if required, such as a furnace (Anton Paar, up to 1100 °C) or a tension, compression machine (Deben, up to 5 kN).

Examples of more special and exotic types of XCT imaging techniques are given in the sections “Differential Absorption Edge XCT” and “Synchrotron X-ray Refraction Computed Tomography”, where these techniques are explained with few examples.

The fields of application of XCT are broadly diversified. For example, in archaeology or cultural heritage, CT is applied to identify materials used and to retrace manufacturing techniques and<sup>[10]</sup> it helps identifying the internal morphology of new fossil species<sup>[11]</sup> or the bony inner ear of baleen whales.<sup>[12]</sup> In biomedicine and biology, CT is used to study dental materials<sup>[13]</sup> or articular cartilages, where true cellular resolution was demonstrated by optimization of phase contrast imaging.<sup>[14]</sup> This was also exploited in unveiling the 3D structural changes of sugarcane bagasse.<sup>[15]</sup> In engineering and materials science, for example, for cast alloys, XCT is currently applied to assess internal damage caused by external loads and to determine volume fractions of constituents in complex multiphase materials.<sup>[16]</sup> Simultaneously, XCT reconstruction techniques are constantly improving as for example new reconstruction algorithms such as Direct Iterative Reconstruction of Computed Tomography Trajectories (DIRECTT)<sup>[17]</sup> have been developed at BAM. DIRECTT is an iterative algorithm based on a sequence of alternating reconstructions and virtual projections of intermediate reconstructions. The basic principle is the computation of line integrals along sinusoidal traces, which correspond to each individual pixel position of the tomogram. In each iteration cycle, predominant pixels are selected, weighed, and added to the intermediate reconstruction of the preceding cycle. The resulting reconstruction is projected and compared to experimental projections. The residual is the input of the following cycle. This is repeated until the residual (sinogram) converges to a predefined

value. Previously, an optimized version<sup>[18]</sup> has been established, which is capable of reconstructing 3D cone beam data.

## 2.1. Fuel Cells and Batteries

Sparked by the activity of some XCT users of the BAMline in the field of energy-related materials and motivated by its mission to safety of materials and devices, HZB and BAM have undertaken fundamental research in the field of fuel cells and Li-ion batteries. In such systems, most of the applied materials possess a complex structure, which influences the ongoing chemical processes. Hence, a detailed look onto the structural changes during operation can give important hints in optimizing materials for future development iterations<sup>[19]</sup> and understanding possible catastrophic failure scenarios.

In the most common type of fuel cells in the automotive industry, the polymer–electrolyte–membrane fuel cell (PEMFC), the water distribution is of great interest as during operation, besides electrical power; also water is produced as a byproduct. This must be removed as it can clog the pathways for the supply gases. Several works are focusing on the water distribution and transport in the porous scaffold materials and how to optimize such materials.<sup>[20]</sup> In most cases, 3D water distributions and its transport paths through the gas diffusion layer (GDL) and the adjoining microporous layer (MPL) are of interest and analyzed during cell operation. For a 3D visualization of the water distribution and the structure of the GDL at different operating conditions in intermittent operation, X-ray tomography was utilized. Based on findings from operando radiography measurements, a water transport pathway with a flow rate of  $22 \text{ pl s}^{-1}$  was detected and then the underlying structure investigated by tomography, see Figure 3. The combination of 2D and 3D techniques allowed a complete 3D visualization of the transport pathways through the GDL and channel structure of both electrodes. Such measurements are typically conducted with pixel sizes from  $0.88$  to  $2.2 \mu\text{m}$  over an acquisition area from  $7 \times 2.5 \text{ mm}^2$  up to  $16 \times 6 \text{ mm}^2$ , depending on the cell design and their purpose. The total scan times range between 30 and 120 min using a monochromatic beam (DMM) with energies between 12 and 20 keV.

In further studies, 3D scans of applied materials were segmented and used as input for modeling the water content.<sup>[21]</sup>

Investigations exploiting the capabilities of synchrotron imaging have also been conducted with high-temperature polymer electrolyte fuel cells (HT-PEFC) and direct methanol fuel cells (DMFCs). In HT-PEMs, the interest is on the distribution of phosphoric acid.<sup>[22]</sup> In DMFCs, additionally to the water evolution on cathode side, also the gas formation of the liquid-filled anode side is of interest, as both products can hinder the supply of educts on both sides.<sup>[23]</sup>

Processes in batteries usually take place on a larger time scale within several minutes or hours. Therefore, besides operando radiography<sup>[24]</sup> tomography is particularly well suited to tackle current problems. XCT is conducted ex situ with extracted materials,<sup>[25]</sup> but mainly operando with batteries, which are cycled at the beamline and imaged 3D with several temporal steps displaying the structure at different states of charge (Zn–air batteries<sup>[26]</sup> and Li batteries).<sup>[27]</sup>

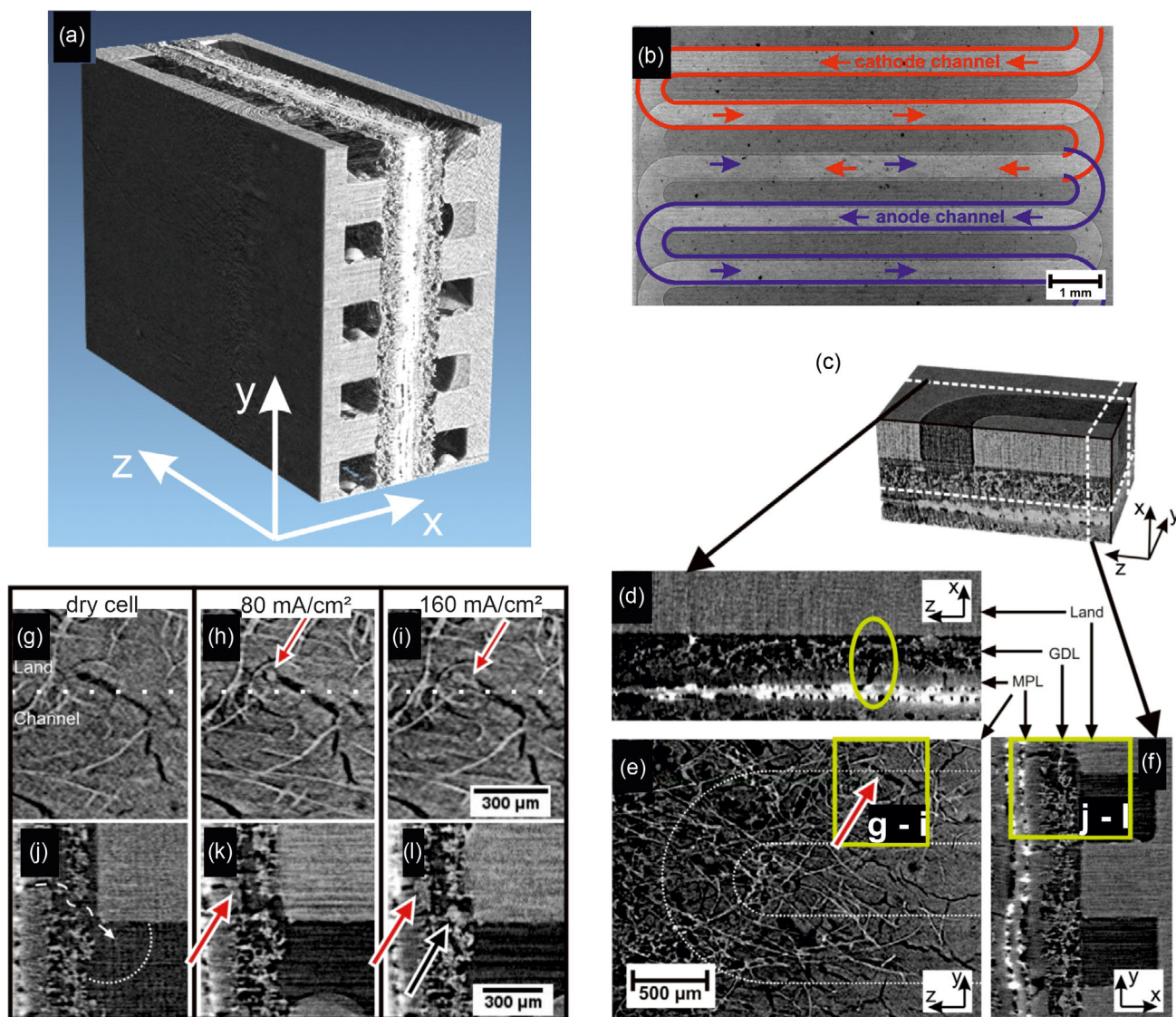


**Figure 3.** a) Investigation of media distribution and transport in a PEMFC. b) A channel system and GDLs provide the electrodes with supply gases ( $H_2$  and air) and must allow for an excess of product water. With radiography (not shown), active transport pathways (red and black arrows) were identified and further studied in 3D by tomography. c–l) At different current densities (g–l), a crack (red arrows) in the MPL has been identified to be the origin of the pathway (Reproduced with permission.<sup>[63]</sup> Copyright 2011, Elsevier).

## 2.2. Additive Manufacturing

In the past years, additive manufacturing (AM) evolved from simple prototyping to the most promising production process used in different industries. The most widespread AM techniques, such as electron beam powder bed fusion (EB-PBF) or laser powder bed fusion (L-PBF), use powder as a raw material. It is well known that powder properties, such as shape, size, and porosity, can have a strong impact on the outcome of the process itself and on the quality of the final component. Therefore, characterization of powder is an important step in understanding and optimizing of the AM and quality control processes.

A synchrotron X-ray CT-study was performed at BAMline aiming for 3D characterization of powders used in LPBF AM.<sup>[28]</sup>

Two different powders were investigated: Ti–6Al–4V produced by plasma atomization and stainless steel 316L produced by gas atomization. High spatial resolution of  $1\ \mu\text{m}$  and large amount of analyzed particles (around 70 000) allowed robust determination of the particle shape and size distributions. A multistep workflow was developed for the segmentation of the individual particles and the analysis of their geometrical features. As a first step, denoising of the reconstructed volume was carried out by an edge-preserving bilateral filter (Figure 4a), followed by an automatic thresholding based on the iterative selection method (ISO) data algorithm.<sup>[29]</sup> An advanced 3D watershed approach (implemented in Fiji ImageJ<sup>[30]</sup>), which tolerates particles' concavity, allowed reliable separation of the particles in contact with each other, this being the most essential step for further analysis (Figure 4b).

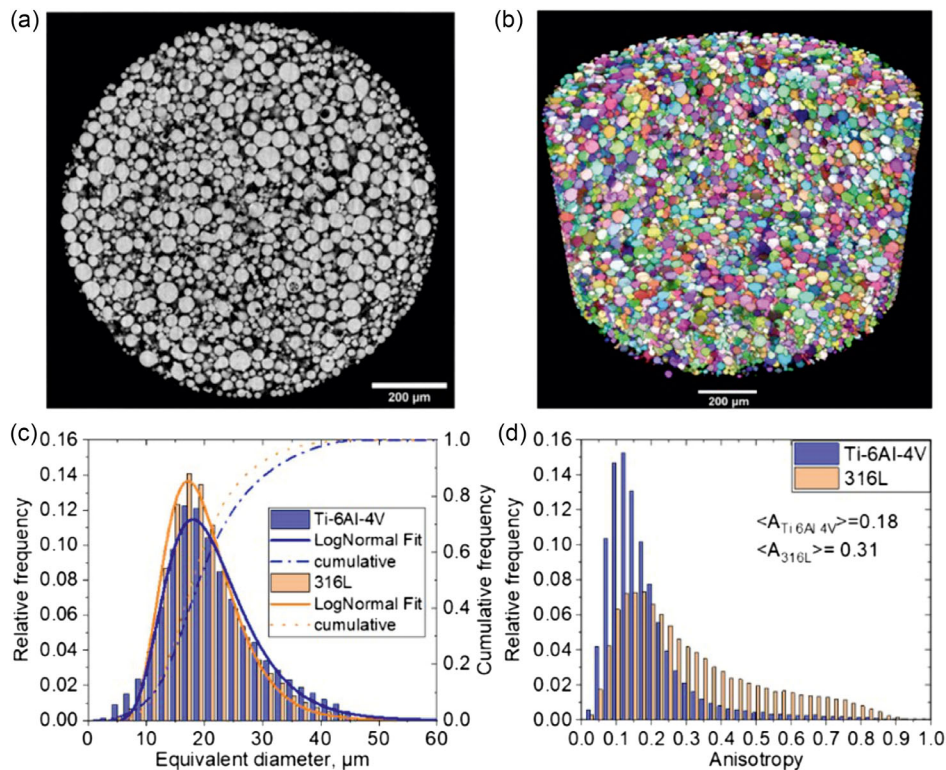


**Figure 4.** a) A reconstructed slice of Ti-6Al-4V powder and b) 3D rendering of the separated powder particles; c) Particle size and d) anisotropy distribution of Ti-6Al-4V and Steel 316L powders (modified from the study by Thiede et al.<sup>[28]</sup>)

The size distribution of the particles (based on equivalent diameter) revealed only a small difference between the two powder types (Figure 4c), showing a larger number of smaller particles in Steel 316L powder. Contrary to the size, the shape of the particles, expressed in terms of anisotropy (based on principal component analysis), was found to be significantly different (Figure 4d). Thus, we proved that different production techniques result in different particles' shape distribution: the plasma-atomized Ti-6Al-4V powder was characterized by more spherical particles than the gas-atomized steel 316L powder. Interestingly, the evaluated packing density of the two powders was almost identical. This indicates that the effect of particle shape on packing density is minor. All experimental results achieved in that study can be used for the optimization of the AM process and as an input for realistic simulations of physical properties (e.g., thermal conductivity) of the powder bed.

### 2.3. Metal Matrix Composites

Aluminum alloys are extensively used in the automotive industry. Particularly, squeeze casting production of Al-Si alloys are well suited for the development of metal matrix composites (MMC), to be possibly employed in combustion engines. An interesting class of MMCs is produced with a random planar orientation of short fibers (SFs), targeting a highly anisotropic mechanical behavior. In order to tailor (reduce) the anisotropy of mechanical properties without a dramatic loss in mechanical performance, the addition of ceramic particles as a second

reinforcement phase has been investigated. The understanding and quantification of load transfer and damage mechanisms in such multiphase (SF + particles) composites are a premise to their optimization (in terms of microstructure and mechanical performance) and thereby to their use in practice.

The study carried out by Evsevlev et al. in 2020<sup>[31]</sup> focused on the characterization of the damage mechanism in composites with single and hybrid reinforcements by means of high-resolution synchrotron X-ray CT. The composites were produced by reinforcing a AlSi<sub>12</sub>CuMgNi alloy with 15 vol% of random planar-oriented Al<sub>2</sub>O<sub>3</sub> SFs (Type I) or with a combination of 7 vol% of random planar-oriented Al<sub>2</sub>O<sub>3</sub> SFs and 15 vol% of SiC particles (Type II). As for simpler Al-Si alloys, eutectic Si precipitates and stiff intermetallic phases also form in the matrix (and therefore appear in both composites). Such precipitate phases play an eminent role in the reinforcement mechanisms.

SXCT experiments were conducted on prestrained samples of Type I and Type II composites: at 5% compressive plastic pre-strain and at failure condition (21% strain for Type I and 13% for Type II). Direct observation of damage after compression tests is exemplarily shown in Figure 5. The volume fraction of microcracks was calculated from the segmented volumes for every compression stage. Different damage mechanisms were disclosed for single- and hybrid-reinforced composites. It was found that the volume fraction of damage is much smaller for Type II (two ceramic reinforcements) than for Type I (solely alumina fibers) at a compressive prestrain of about 5%, indicating that Type II is able to accommodate strain more efficiently in the

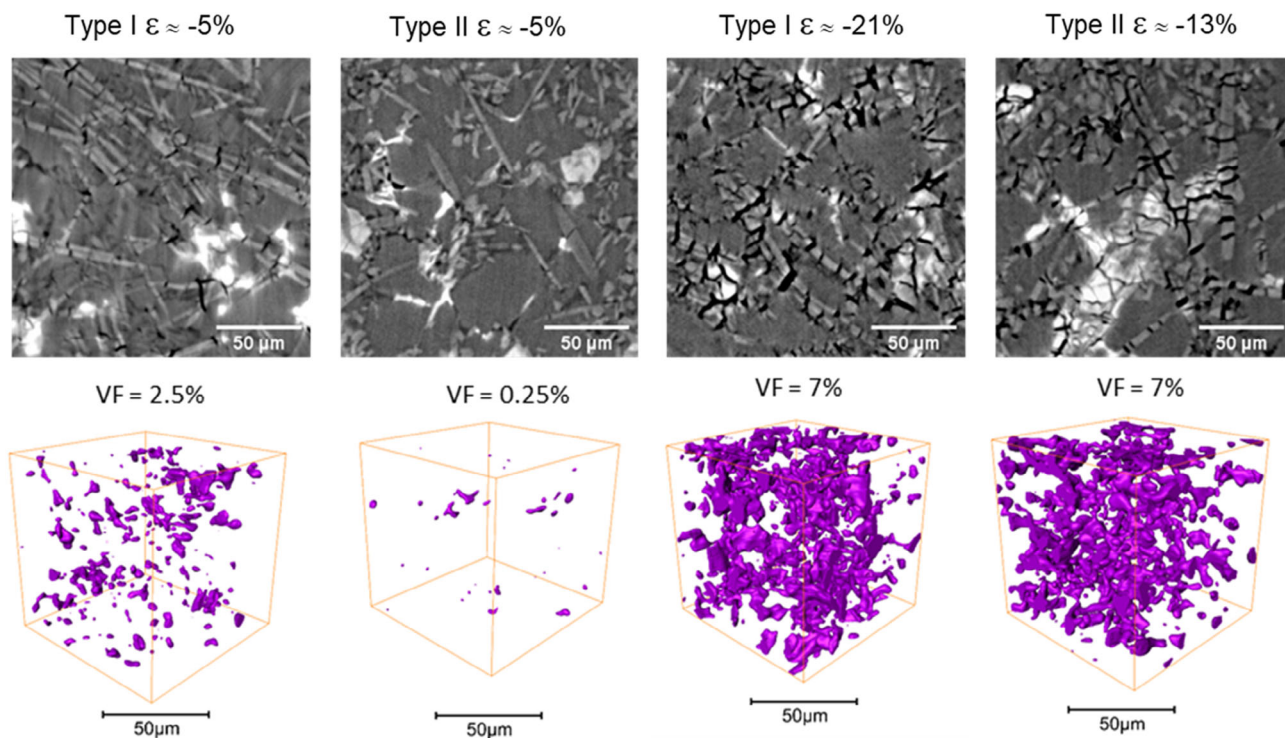


**Figure 5.** Top row: reconstructed slices of Type I and Type II composites at different prestrains. Bottom row: 3D rendering of the segmented damage (microcracks). Adapted with permission.<sup>[31]</sup>

low-plastic strain region. However, at failure, both composites reach a similar volume fraction of damage, while Type I fails at almost double the strain than Type II. This indicates a more catastrophic development of damage as a function of applied pre-strain. It was observed that cracking of SiC clusters in Type II plays a crucial role: since SiC particle clusters have low aspect ratio, one can think that their rupture is “simultaneous”, since the radial stress component is always normal to the main axis of some clusters. These results, in combination with load transfer analysis made by neutron diffraction experiments (see other studies<sup>[16,31,32]</sup>), are particularly important for the optimization of the MMC composition and can be used as an input to analytical and numerical models for prediction of their micromechanical behavior.

### 3. Differential Absorption Edge XCT

The attenuation coefficients decrease with rising incident beam energy. Such continuous function has discontinuities at the absorption edges. Absorption edges correspond to beam energies that can excite a certain electronic state of the investigated material. As the electronic states differ from element to element, exploiting the absorption edges allows element-sensitive tomographic imaging, sometimes called “differential absorption edge XCT”. The DMM installed at the BAMline delivers a spectral band narrow enough to conduct imaging below and above some absorption edge of a certain element with good energy resolution. The attenuation difference above and below the edge is

exploited to localize some elements and map their 3D spatial distribution. As the DMMs (and beamline) energy range is between 8 and 60 keV, any element with absorption edges in this range can be studied, provided the overall sample contrast and transmission are suitable. Typical elements, which can be suitably studied at the BAMline, are copper and ruthenium, as demonstrated below.

#### 3.1. Additively Manufactured Metal–Organic Frameworks

In the past two decades, a whole variety of different metal–organic frameworks (MOFs) of different sizes, functionalities, and structures have been developed. This subclass of coordination polymers consists of metal ions coordinated to organic ligands. The porosity of many MOFs enables new possible applications in fields such as catalysis or gas storage.<sup>[33]</sup> MOFs produced by AM possess enhanced applicability due to the increased freedom of component design. The distribution of the AM MOF HKUST-1<sup>[34]</sup> within a polymer matrix made of acrylonitrile butadiene styrene has been studied via absorption edge tomography at the Cu-K-edge by Scholz et al.<sup>[35]</sup> SXCT reconstructions are shown in **Figure 6**. The specimen was scanned at 8.8 keV, slightly below the Cu-K-edge, and at 9.2 keV, slightly above it (the Cu-K-edge is located at 8.98 keV). As a result, the attenuation of copper differs in the two scans, whereas the rest of the materials exhibit only small negligible changes. The two data sets were fused via a machine learning algorithm in order to extract the copper distribution. The data treatment process is shown in **Figure 6**.

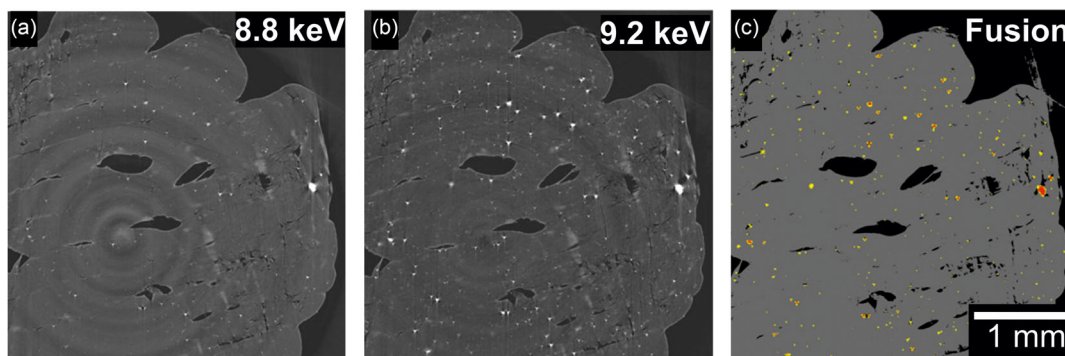


**Figure 6.** Tomographic slices of the 3D-printed cylinder at a beam energy of a) 8.8 keV, b) 9.2 keV, and c) the result of the data fusion of the two slices exploiting the absorption edge of copper at 8.98 keV (Reproduced with permission.<sup>[35]</sup> Copyright 2020, De Gruyter.).

Data fusion enhances redundant features of the two datasets while suppressing features that differ between the datasets (e.g., reconstruction artefacts).<sup>[36]</sup> It requires a pixel-correct registration of the two datasets onto each other. The separate acquisition of the two datasets (at different energies) results in two gray values for each pixel. Such gray values can be projected as a 2D histogram plane for each slice of the dataset; each axis represents the gray levels of one of the datasets. In this 2D fusion space, gray values of the same material form point clusters that can be segmented by machine learning algorithms. Using this approach enabled the segmentation of four classes in the datasets: air, polymer matrix, dense clusters of copper particles, and loose clusters of copper particles. The unsupervised machine learning algorithm Gaussian mixture model was used.<sup>[37]</sup> Figure 6c) shows the four classes color coded. Interestingly enough, a complete suppression of ring artefacts is obtained by the data fusion process. The study has shown that AM cylindrical specimens as well as the feedstock filament itself possessed a homogeneous distribution of copper in the MOF on a length scale of 100  $\mu\text{m}$ ; from the technical point of view, this would enable an optimum adsorption capacity.

### 3.2. Direct Methanol Fuel Cell Catalysts

The continuous loss of power output of a fuel cell primarily depends on aging effects in its components. Hereby, the active surface area of the catalyst layers plays a crucial role. Especially

the oxygen reduction reaction, taking place in the anode electrode, is a limiting factor for the overall cell performance. To counteract this limitation, a mixture of platinum (Pt) and ruthenium (Ru) is used for DMFCs. By means of differential absorption edge tomography, it was shown that the catalyst ruthenium undergoes a redistribution between areas below channels and below ribs of the flow-field structure.<sup>[38]</sup> For the tomographic investigations, pristine and aged samples were prepared from a fuel cell membrane electrode assembly (MEA) and examined ex situ.

It was shown that these redistributions can be attributed to mass transport (gas and liquid) in the MEA and the structure of the GDL (twill fabric). The catalyst contained Pt and Ru as a mixture. With conventional absorption imaging, it is not possible to distinguish between the two elements, since their atomic number is similar. Hence, since Ru has its K-edge at about 22.1 keV (i.e., in the energy range accessible at the BAMline), two scans, one above the Ru-K-edge at 22.0 and one below the edge, at 22.2 keV, were conducted for a differential absorption edge tomography. Dividing the two datasets delivered the Ru distribution only. This is shown in red color in **Figure 7**. The GDLs, which were made of carbon fibers, are shown in gray. A superposition of the two, GDL and Ru, distributions showed the correlation between the fiber arrangement and the Ru distribution (Figure 7e). It was found that the catalyst preferentially clusters at the crossing regions between fiber bundles.

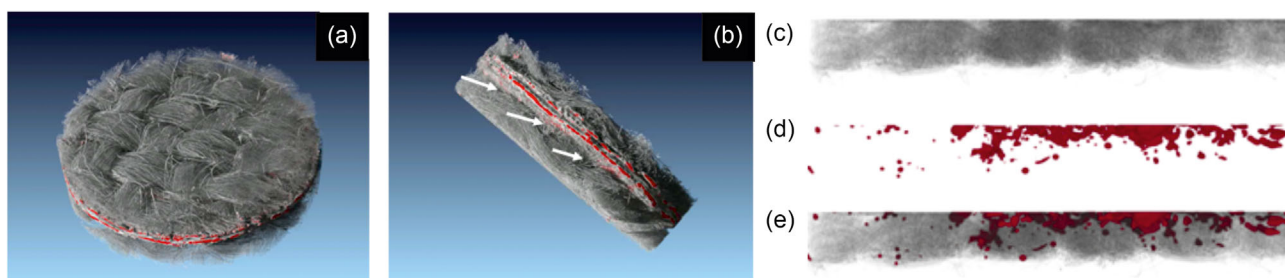


**Figure 7.** a) Ex situ differential absorption edge tomography of a 3 mm-diameter MEA of a DMFCs (Reproduced with permission.<sup>[38]</sup> Copyright 2011, Elsevier). A 3D rendering of the whole assembly and b) white arrows pointing to gaps due to the arrangement of the fiber bundles. c) Side view of only the fibers, d) only the ruthenium distribution, and e) fibers and ruthenium.



### 3.3. Detection of Stained Organic Material in Soil

Since it impacts our daily life, agriculture is an ongoing field of research. In fact, the increasing population on Earth requires reliable food production. Simultaneously, desertification and soil erosion increase in certain regions due to the climate change. Thus, soil stabilization and a functional ecosystem are urgently needed to keep the harvest at a high level. Both problems can be addressed by implementing fungi into the soil. Depending on the species, it can stabilize soil particle, allowing roots to grow more stable and efficient. Also, the water storage capability of the soil can be increased since porosity, aggregation and particle density are impacted by the fungal hyphae. Soil organic matter (SOM) is essential for the ecosystem and the carbon storage capability of the soil. Soil carbon storage in soil is a complex process that especially involves microbial activity. Thus, 3D analysis of the distribution of fungi, soil particles, and SOM is essential to understand the working principles and mechanical properties of this ecosystem.

Both fungi hyphae and SOM mainly consist of carbon and therewith can hardly be distinguished by X-ray tomographic analysis. To increase the contrast between the two organic materials, Lammel et al. stained a whole sample with iodine ( $I_2$ ), which mostly interacts with SOM instead of the fungi material.<sup>[39]</sup> Differential absorption edge tomography at the  $I_2$ -K-edge

(33.2 keV) finally emphasized the SOM, see Figure 8c. This is rendered in cyan color in Figure 8d. To prove the interaction, two control samples, taken from the same source, but without staining, were additionally prepared. These samples did not show  $I_2$  agglomerations in SOM, see Figure 8a,b.

## 4. Synchrotron X-ray Refraction Radiography (SXRR)

X-ray refraction is an excellent tool for the characterization of the microstructure of materials. However, there are only a few (synchrotron) laboratories in the world that use this technique for material characterization. Therefore, we first explain the basic principles and the measurement techniques before presenting application examples.

X-ray refraction occurs when X-rays interact with interfaces between materials of different densities. It is based on Snell's law and is analogous to the refraction of visible light by lenses and prisms. The major difference between visible light and X-rays is that the refractive index  $n$  of X-rays in matter is slightly smaller than 1 (by about  $10^{-5}$  to  $10^{-7}$ ). This causes ray deflections of very small angles<sup>[40]</sup> (from a few seconds to a few minutes of arc). Although refraction of X-rays has been observed as early as in the 1920s,<sup>[41]</sup> only in 1987 it was introduced for

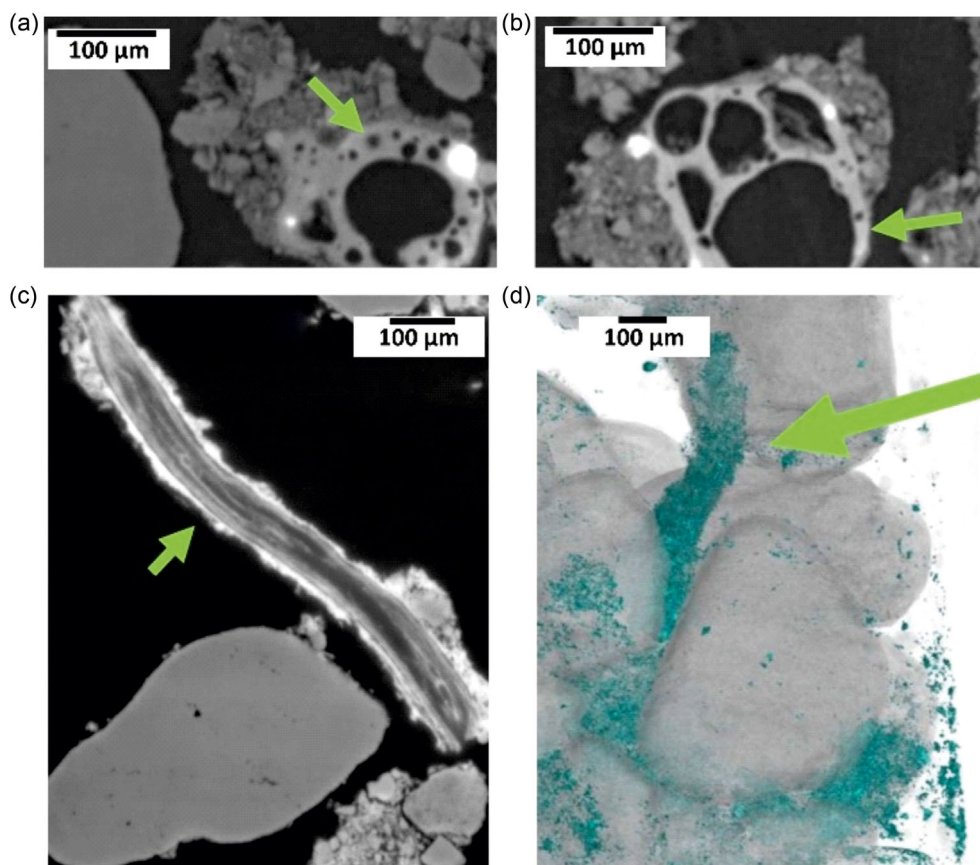


**Figure 8.** a,b) Soil control samples without  $I_2$  staining. c) Cross section of sample stained with  $I_2$ , the SOM (green arrow) is thereby highlighted. d) 3D view of same sample.

materials characterization and nondestructive testing.<sup>[42]</sup> The measured refraction signal is proportional to the internal specific surface  $\Sigma$  (i.e., surface per unit volume).<sup>[42,43]</sup> In general, interfaces, where the X-ray refractive index  $n$  has discontinuities, will lead to refraction. This technique is extremely suitable for the examination of defects such as cracks and pores as soon as they exceed a size or opening of a few X-ray wavelengths. Since the typical X-ray wavelengths are  $\approx 0.1$  nm, the smallest detectable object size is down to the nanometer range. This is not to be confused with the spatial resolution or the size of the objects that can be imaged. The spatial resolution is limited by the pixel size of the detector system. In other words, nanometric objects can be detected but not necessarily imaged one by one. It must be also emphasized that because of the inevitable background noise, it is impossible to conclusively detect one single defect. Rather, a certain population of objects is necessary to yield an integrated signal above the background noise. Another property of the refraction effect is that the deflected radiation lies in the plane spanned by the interface normal and the vector of the original direction of propagation of the radiation. This means that the propagation direction of the radiation deflected by refraction depends on the orientation of the interface.

X-ray refraction is primary used in radiographic mode with thin specimens (platelets) and yields 2.5D information on the microstructure of the specimen (2D lateral resolution corresponding to the size of the detector pixels and signal integration along the specimen thickness  $t$ ). This results in the detection and mapping of a population of defects rather than the imaging of single defects.

To perform synchrotron X-ray refraction radiography (SXRR), a highly collimated and monochromatic X-ray beam from a double-crystal monochromator (DCM) provided by Si(111) crystals is used.<sup>[44]</sup> The beam energy is adapted to achieve a specimen transmission of about 10–25%. The DCM provides the necessary vertical parallelism/divergence for the measurements and has an energy bandwidth of  $\Delta E/E = 0.3\%$ . A 0.2 mm-thick beryllium filter is placed in front of the DCM to minimize the heat load on the first crystal. The accessible photon energy range extends from 8 to 55 keV. The detector system currently in use consists of a pco.1600 camera and a lens system that images a CdWO<sub>4</sub> fluorescent screen onto the camera's light-sensitive CCD chip. The pixel size can be adjusted to the requirements of the experiment using the existing lens combination and ranges from 0.82 to 4.08  $\mu\text{m}$  (see Table 2). The transmission thickness of the samples depends on the material and ranges from 1 cm for C-fiber composites ( $E = 20$  keV) to 0.2 mm for steel ( $E = 50$  keV). The size of

the samples depends on the field of view. For sample plates larger than the FoV, the measurements can be stitched.

In contrast to absorption-based radiographic measurements, a Si (111) analyzer crystal is placed in the beam path between the specimen and the detector, as shown in Figure 9 (left). The analyzer crystal reflects to the detector only those rays that impinge on it at the Bragg angle  $\Theta_{\text{Bragg}}$  (e.g.,  $\Theta_{\text{Bragg}} = 2.2664^\circ$  at 50 keV). By tilting the analyzer crystal around the Bragg angle, the so-called rocking curve (RC) is recorded (see Figure 10). A radiograph with and without the specimen in the beam is taken at each of the typically 50 angular positions of the crystal. Thus, rocking curves are obtained for each pixel of the detector. Such curves describe the dependence of the intensity of the reflected beam as a function of the deviation from the Bragg angle,  $\Delta\Theta_{\text{Bragg}} = \Theta - \Theta_{\text{Bragg}}$ . Figure 10 shows three rocking curves: The curve with the blue open circles shows the measurement without specimen in the beam (flat field). The integral of the curve corresponds to the intensity and the full width at half maximum (FWHM) to the intrinsic divergence of the incident beam. The curve with the green-filled triangles shows the measurement with a specimen in the beam that features internal interfaces. The integral of this curve corresponds to the transmitted intensity while the FWHM is proportional to the amount of the internal interfaces in the specimen. The more internal interfaces the specimen has, the greater the FWHM. The curve with the gray open triangles represents the rocking curve one would measure if the specimen had no interfaces. Its FWHM would be identical to that of the blue curve (there are no internal interfaces at which the X-ray beam is deflected). Since refraction corresponds to pure redistribution of beam (leaving the integral unchanged), a sample with internal interfaces causes broadening of the RC on the expense of decreasing peak height. The integral would be identical to that of the green curve (the absorption of a specimen is independent of the presence of internal interfaces). This means that the peak height is an indirect measure of the rocking curve's broadening due to inner surfaces.

Using an in-house developed Python 3.0-based software, the rocking curve is fit by a pseudo-Voigt function for each detector pixel.<sup>[45]</sup> The curve parameters  $I_0$  (curve integral without specimen in the beam),  $I$  (curve integral with specimen in the beam),  $I_{R0}$  (the curve maximum without specimen in the beam), and  $I_R$  (curve maximum with specimen in the beam) are determined from the fitting and saved as gray value 2D images. Using the image analysis software "Fiji Image J",<sup>[46]</sup> the local attenuation properties  $\mu \cdot t$  and the local refraction values  $C_m \cdot t$  can be evaluated for each pixel according to Equation (1) and (2), respectively. For a detailed description of data processing and evaluation the reader is referred to<sup>[47]</sup>

$$\mu \cdot t = -\ln\left(\frac{I}{I_0}\right) \quad (1)$$

$$C_m \cdot t = 1 - \frac{I_R}{I_{R0}} \cdot \frac{I_0}{I} \quad (2)$$

This analysis can be made on specimens of macroscopic size (say a few cm), that is, the FoV of X-ray refraction techniques is much larger than that of high-resolution XCT and of classic microscopy.

**Table 2.** Effective pixel size and FoV for different camera objectives.

objective	nominal pixel size [ $\mu\text{m}$ ]	field of view [ $\text{mm}^2$ ]
20 $\times$	0.82	1.3 $\times$ 1.0
50 $\times$	1.92	3.1 $\times$ 2.3
100 $\times$	4.08	6.5 $\times$ 4.9

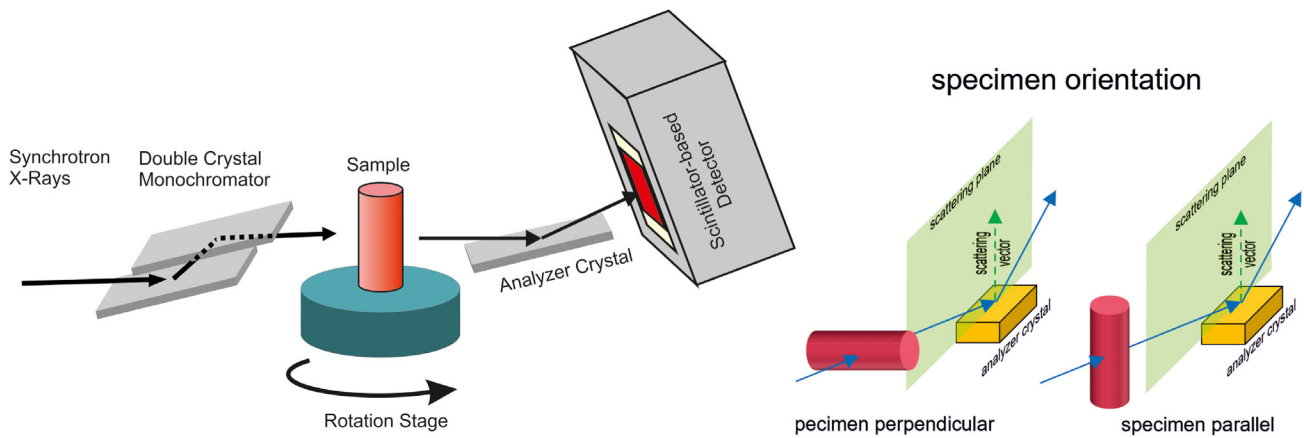


**Figure 9.** Left; sketch of the experimental setup of the X-ray refraction station at BAMline. Sample rotation can be used for X-ray refraction tomography (see below). Right; specimen orientation with respect to the scattering plane of the analyzer crystal.

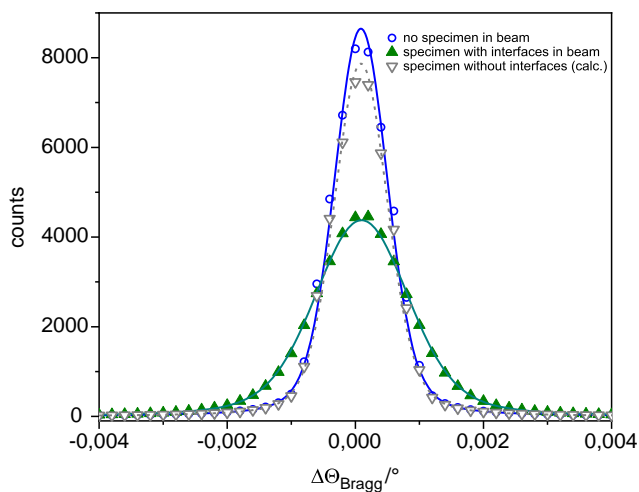


**Figure 10.** Measured rocking curve of the incoming synchrotron X-ray beam, that is, without any specimen (blue open circles), after transition through a specimen without internal surfaces (gray open triangles) and after transition through a specimen with internal interfaces (green-filled triangle). To record the curves, the analyzer crystal is rotated stepwise around the axis perpendicular to its scattering plane (the scattering plane is spanned by the incident and outgoing beam vectors, see Figure 9).

In addition, X-ray refraction methods are sensitive to defect orientation due to the presence of the analyzer crystal. The analyzer crystal only discriminates the X-rays within its scattering plane (Figure 9 right) and, therefore, only interfaces whose surface normal is oriented within the scattering plane, with a tolerance of about  $\pm 45^\circ$ , can be detected and provide refraction intensity to the rocking curve. An isotropic inhomogeneity, such as a spherical cavity, would provide signal for any specimen orientation with respect to the scattering plane. In the case of cracks or elongated pores, however, a signal is detected only if the surface of the crack or cylindrical pore is oriented perpendicularly to the scattering plane. This means that the refraction intensity is dependent on the orientation of the specimen with respect to the

scattering plane of the analyzer crystal and can therefore be used to identify the type of defect and its orientation. For example, the effects of the manufacturing process<sup>[48]</sup> or of the external load on the specimen<sup>[49]</sup> have been investigated (they both induce anisotropy of defects). **Figure 11** impressively shows the potential of SXRR compared to absorption-based radiography using the example of an AlMgSi weld seam. Both radiograms were taken with the same detector (pixel size  $3.5 \mu\text{m}$ ). The left image shows the linear absorption ( $\mu \cdot t$ ) of the specimen. Cracks as well as a pore can be seen as dark gray fields and as a disc. The right image shows the same recording, but with the analyzer crystal at the center of the rocking curve. Since all deflected (here: refracted) rays are not reflected by the analyzer crystal in its  $\Theta_{\text{Bragg}}$  position, the numerous cracks in the weld cause additional image contrast (see dark areas). Here, too, the crack fields and the pore can be seen as in the left-hand image, but beyond that there are countless cracks that are not visible in absorption mode. The sensitivity of the refraction setup to the orientation of the interface can be seen very well in the example of the pore. The upper and lower interfaces of the pore appear as dark crescents because the analyzer crystal does not reflect to the detector all rays that propagate parallel to its scattering plane and do not strike it at the Bragg angle. The left and right interfaces of the pore are almost invisible, since here the direction of propagation of the rays deflected by refraction is perpendicular to the scattering plane of the analyzer crystal.

The X-ray refraction signal can be quantitatively correlated with microstructural changes and coupled with the predictions of micromechanical models.<sup>[43,50]</sup> The influence of the specimen thickness  $t$  is eliminated by dividing the local refraction value  $C_m \cdot t$  by the local absorption property  $\mu \cdot t$  (see Equation (1) and (2)) This yields the relative specific refraction value  $C_m/\mu$ , which is correlated to the relative specific (internal) surface of the specimen. Absolute values can be determined if an instrument calibration is performed by means of a calibration specimen with known specific surface and identical absorption properties. In most cases, this time-consuming calibration procedure is not necessary since the relative damage evolution of a material is the quantity of interest.

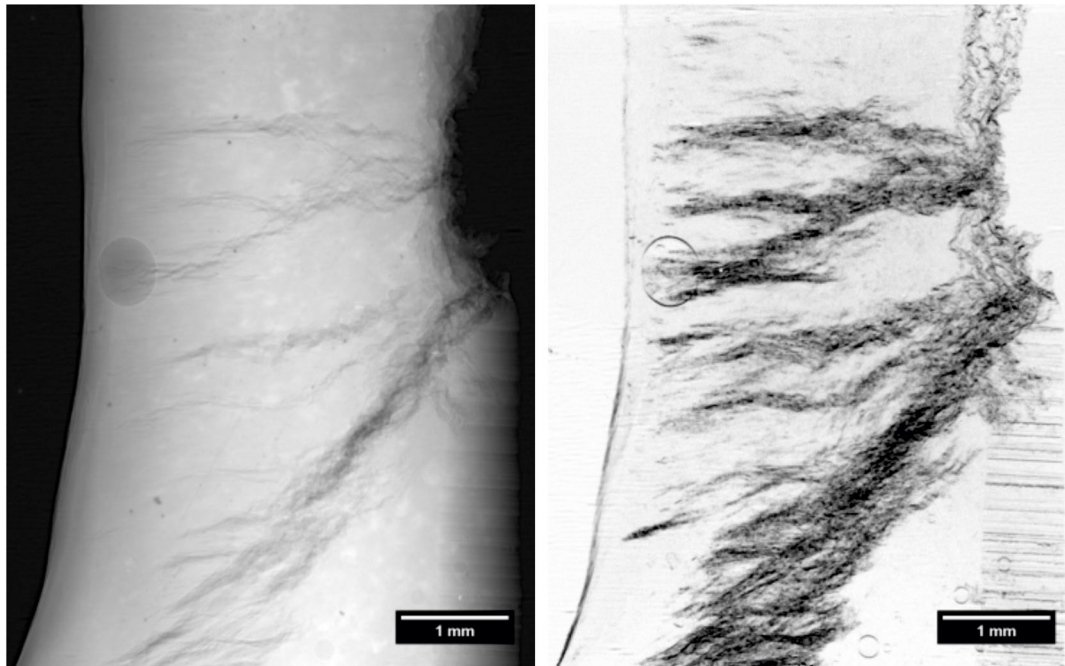


**Figure 11.** Comparison of a conventional absorption-based radiograph ( $\mu\cdot t$ , left) and a SXRR image ( $I_R$ , right) of an AlMgSi weld seam. Due to SXRR's sensitivity to interfaces, cracks are contrasted much higher.

The main drawback of SXRR is the limited sample thickness: if we increase the photon energy, the refraction signal fades away, and the refraction angle becomes too low. Challenges in SXRR concern the use of the technique for in situ investigations and the quantification of features in tomographic mode.

#### 4.1. Cordierite Diesel Particulate Filter Materials

Porous synthetic cordierite is an attractive ceramic material commonly used for diesel particulate filters (DPFs)<sup>[51]</sup> and refractories.<sup>[52]</sup> Among its properties, the anisotropy of the thermal expansion (see. e.g., the study by Bruno et al.<sup>[53]</sup>) is widely used to tailor the thermal and mechanical properties. Besides the properties of the solid phase, one of the most important features to take into account when evaluating the mechanical or filtration performance of these materials is the pore space morphology and orientation (note that it is incorrect to speak about pores in such bicontinuous materials). The SXRR technique is ideally suited for these types of investigations.<sup>[54]</sup> In small single-walled slabs (called S1 and S2) of two commercial cordierite DPF, ceramic honeycomb filter materials were used for this application. **Figure 12** shows the measurement results for both specimens in two orthogonal orientations with respect to the extrusion axis. While, as expected, the  $\mu\cdot t$  values are independent of the sample orientation (compare Figure 12a,d), the interface between the pores and the solid matter shows a preferential orientation along the extrusion axis (compare Figure 12b,e and c,f, respectively). The porosity fraction and the (fictitious) mean pore size determined by mercury porosimetry confirm the interface density ratio between the two cordierite samples found with SXRR. Interestingly enough, the pore space orientation factor

determined by SXRR (about 1.2 for both specimens) is in good agreement with reported crystal texture values.

Such correlation has been also extended to other porous ceramics, such as aluminum titanate and SiC.<sup>[55]</sup>

#### 4.2. Evolution of Thermal Microcracking in Refractory $ZrO_2$ - $SiO_2$

Zirconia-based cast refractories are widely used for glass furnace applications. Since they have to withstand harsh chemical as well as thermomechanical environments, internal stresses and microcracking are often present in such materials under operating conditions (sometimes in excess of 1700 °C). The manufacturing of high-quality glasses required for new applications (e.g., flat panel liquid crystal display (LCD) or plasma display panels) implies the development of new, high-zirconia fused-cast refractories with excellent thermomechanical properties. In this case study,<sup>[56]</sup> the evolution of thermal (coefficient of thermal expansion) and mechanical (Young's modulus) properties as a function of temperature and applied preload in a fused-cast refractory  $ZrO_2$ - $SiO_2$  composite was investigated. With the aid of SXRR (yielding the internal specific surface in materials), the evolution of microcracking as a function of thermal cycles (crossing the martensitic phase transformation of  $ZrO_2$  around 1000 °C) under externally applied stress was monitored. **Figure 13** shows the local relative specific refraction value  $C_m/\mu$  as 2D color-coded images, for the load direction oriented perpendicular and parallel to the scattering plane of the analyzer crystal for each specimen. The color spread is the same for all images. It was found that external compressive stress during the thermal cycles leads to a strong decrease of the room-temperature internal surface

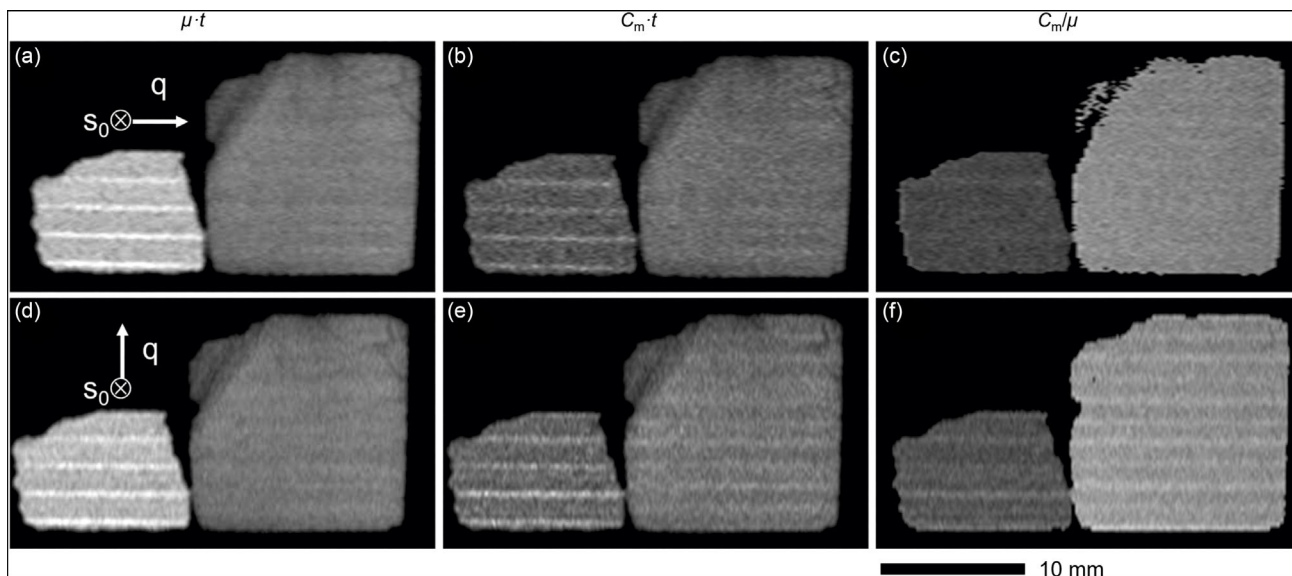


**Figure 12.** 2D mapping of single wall slabs of cordierite samples. Large slab from sample S1, small slab from sample S2, respectively. The horizontal footprints indicate the extrusion direction. Top row: scattering vector  $\mathbf{q}$  (nearly) parallel to extrusion, bottom row: scattering vector  $\mathbf{q}$  perpendicular to extrusion. The incident beam direction  $\mathbf{s}_0$  is also indicated. a,d) The gray values correspond to: absorbing mass, b,e) volume-related specific surface, and c,f) mass-related specific surface. Reproduced with permission.<sup>[54]</sup> Copyright 2013, Göller.

per unit volume (see Figure 13 bottom left –5 MPa), but a tensile load has a similar (though not-so-strong) effect (see Figure 13 top right 1 MPa). In agreement with existing literature on  $\beta$ -eucryptite microcracked ceramics,<sup>[57]</sup> we could explain these phenomena by microcrack closure in the load direction in the compression case and by microcrack propagation (rather than microcrack nucleation) under tensile conditions.

#### 4.3. Damage to Fiberglass in Endodontic Posts Following Dental Bur Trimming

Dental fiberglass posts are composites made of axially aligned glass fibers bound together with a polymer matrix. In dentistry, fiberglass dental posts are used as flexible and light reinforcements to support postendodontic restorations, benefiting from the high strength of the millimeter-long glass fibers with micrometer diameters. Dental posts are used for tooth restoration following root canal treatment and extensive tooth tissue destruction (e.g., by caries). Posts are placed in and bonded to the cleared root canal where they contribute to mechanical retention of artificially restored dental crowns. Fiberglass posts are usually mass produced in standard lengths and thicknesses. Thus, to fit roots with biologically varying anatomies, the post must be trimmed. The effects of trimming fiber-glass posts are poorly understood. There is concern that the integrity of fiberglass dental posts may be affected by chairside trimming during treatment. In the study reported here,<sup>[58]</sup> SXRR was applied to reliably identify and characterize the extent of damage caused by trimming. Figure 14 shows grayscale images of the relative specific surfaces ( $C_m/\mu$ ) of the control, grooved, and beveled posts, respectively. The maps reveal local variations in interfaces and highlight specific regions containing submicrometer damage/internal surfaces; such damage depends on the orientation

of the specimen with respect to the analyzer scattering plane. The stronger signal is quantitatively depicted in the grayscale values, which show significantly higher scattering originating from the dominant interfaces oriented parallel to the glass fibers in all three posts (Figure 14a–c left, i.e., for the perpendicular orientation). The mean value of the relative specific surface in this post orientation is  $\approx 4$  times higher than the mean value measured parallel to the glass fiber orientation (Figure 14a–c right, interfaces perpendicular to the fibers). In other words, substantial scattering takes place along the interfaces between the reinforcing glass fibers and the matrix. The mean  $C_m/\mu$ -value of “regular” post regions is about 0.38 and varies from 0.27 in the dark to 0.67 in the brighter stripes. Dark stripes indicate areas with better fiber matrix bonding, and light areas suggest local defects in bonding. The fact that for the most part posts in the parallel orientation (Figure 14a–c right) show a very low  $C_m/\mu$  ratio of about 0.05 suggests that almost no internal inhomogeneities are oriented perpendicular to the main fiber axis. This means that both the matrix and the glass fibers are continuous with negligible pores and cracks. The damage caused by the drill is clearly visible in both orientations of the posts. The bright halos suggest that damage encompasses a volume extending at least 50  $\mu\text{m}$  away from the surface that came into contact with the dental drill. Due to the extent of damage and possible consequences to restoration integrity, it might be best not to trim fiberglass posts and produce them tailored to the patient’s need.

#### 4.4. Distinguishing Unprocessed Powder from Empty Pores in Additively Manufactured Ti–6Al–4V

The L-PBF AM technique is a powerful tool for manufacturing near-net-shape and lightweight components in a time-efficient and resource-saving manner. AM requires no molds or

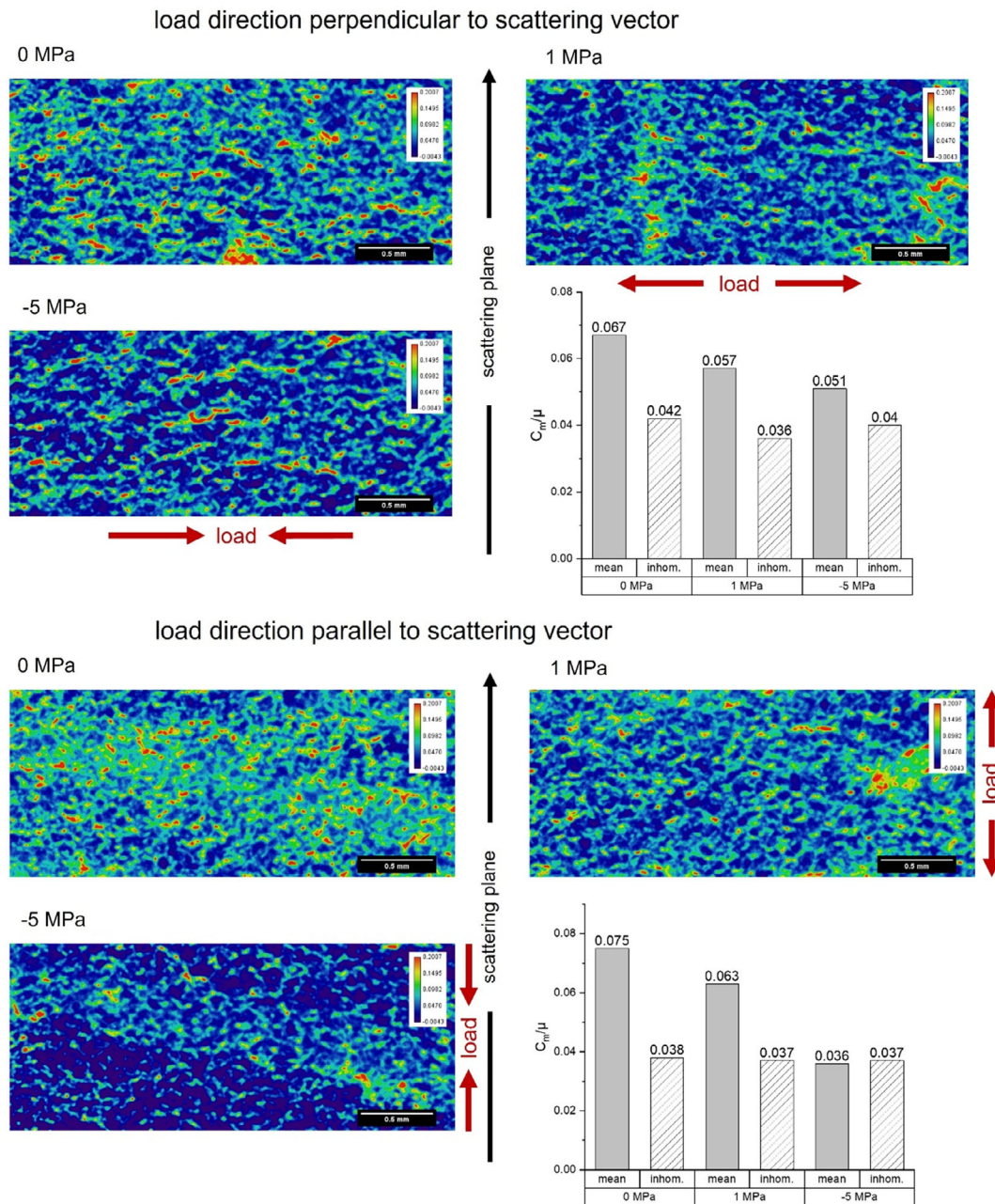


**Figure 13.** Visualization of the local values of the relative specific refractive value  $C_m/\mu$  as 2D color-coded images. The load direction of the specimen was perpendicular (top) and parallel (bottom) to the scattering plane of the analyzer crystal, respectively. 0 MPa: unloaded temperature cycle, 1 MPa: tensile loaded, -5 MPa: compression loaded. The integral values of the relative specific surface for the specimens are shown as bar graphs. The hatched bars represent the inhomogeneity of the  $C_m/\mu$  values across the measured area of the specimen. Reproduced with permission.<sup>[56]</sup> Copyright 2019, MDPI.

part-specific tools and enables the fabrication of very complex and customized parts directly from computer-aided design (CAD) models. In particular, the Ti-6Al-4V (Ti64) alloy is mostly used in the aerospace industry and very widespread in the medical field. However, the rapid solidification during L-PBF and non-optimal process parameters may cause instabilities during the process. Such instabilities lead to the formation of inner defects in the parts: binding or fusing faults, balling, keyhole defects, and even crack formation from thermal residual stress. In this

study we report,<sup>[59]</sup> X-ray refraction techniques were used for the identification of void formation in L-PBF Ti-6Al-4V parts. The topology and volume fraction of pores were measured in samples produced with different laser energy densities,  $E_v$ . In fact, different kinds of defects appear if  $E_v$  lies below or above the optimum laser energy density; unmolten powder particles, balling effect, and fusion defects appear if  $E_v$  is too low, empty keyhole pores appear if  $E_v$  is too high. Since with X-ray refraction it is possible to detect small inhomogeneities (voids or cracks)

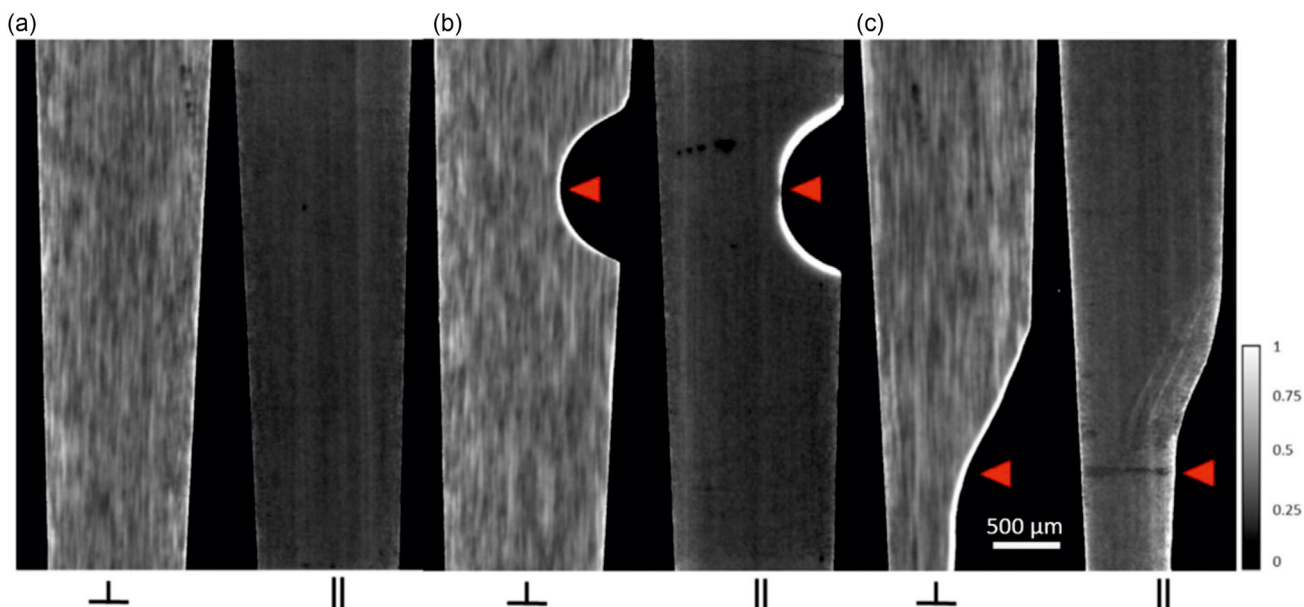


**Figure 14.** Grayscale images of the relative specific surface ( $C_m/\mu$ ) obtained from SXRR measurements in perpendicular ( $\perp$ ) and parallel ( $\parallel$ ) orientations of the dental posts with respect to the scattering plane of the analyzer crystal (see Figure 9). Note the large difference in the gray values (by a factor of up to 4) between the two orientations of each sample. Significant scattering takes place between structures oriented along the fiber axis. The a) control sample demonstrates the typical appearance of an as-received post. Intensity patterns corresponding to the fibrous structures of the post create faint vertical lines due to slight variations in matrix thickness. The grooved b) and the beveled c) samples were trimmed with a high-speed dental drill, removing material in the regions marked by red arrows. A strong bright signal along the surface affected by the drill and is due to a high local concentration of newly formed internal surfaces (possibly microdamage). Reproduced with permission.<sup>[58]</sup> Copyright 2021, Elsevier.

with sizes below the spatial resolution of optical microscopy and XCT, we demonstrated such capabilities to tackle such a challenging problem.

Figure 15 shows the 2D distributions of the specific surface and the local porosity integrated over the thickness of the

specimen (note the different grayscale of each subfigure). The two main messages are as follows: 1) SXRR detects more defects than X-ray transmission radiography in both samples (specimen 1 =  $E_v$  below and specimen 2 =  $E_v$  above the optimal values). In both specimens, defects are aligned perpendicular to

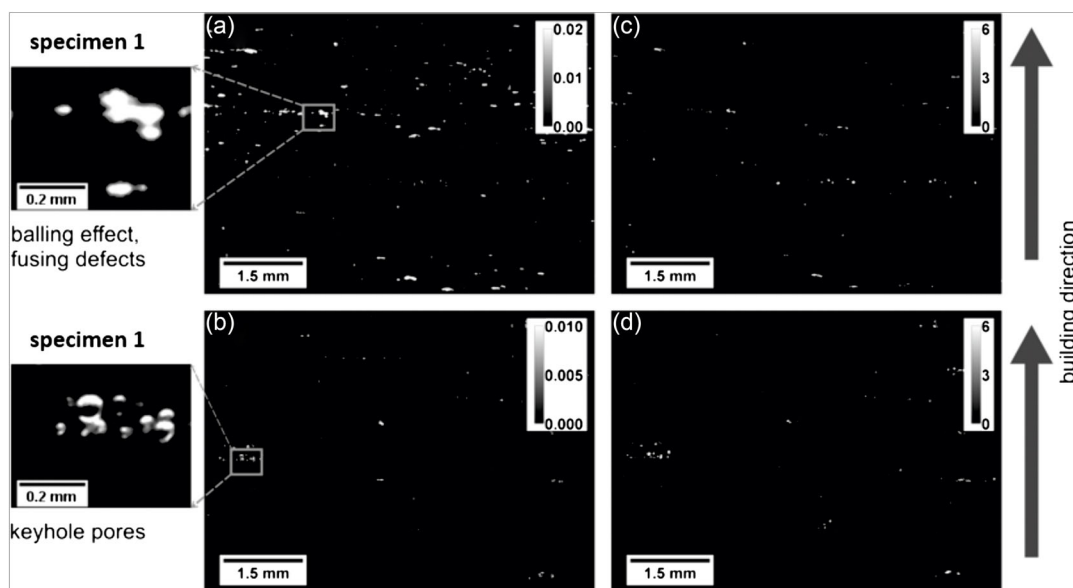


**Figure 15.** (Left) 2D distribution of the specific surface in  $\text{mm}^{-1}$  of a) specimen 1 and b) specimen 2 from SXRR; (right) 2D distribution of porosity in % of c) specimen 1 and d) specimen 2 from conventional radiography. Reproduced with permission.<sup>[59]</sup> Copyright 2018, AIP Publishing.

the building direction (vertical direction in Figure 15) and are located between successive layers. Some 247 defects were found by SXRR against 85 found by transmission radiography for specimen 1; analogously, 119 defects were found by SXRR against 96 by transmission radiography for specimen 2. Both, transmission radiography and SXRR, have been performed with identical spatial resolution. Therefore, it can be concluded that the defects additionally detected by SXRR are smaller than the actual spatial resolution. 2) There are clearly two types of defects that can be distinguished in the SXRR images. One type is shown in the enlarged detail of Figure 15a for specimen 1. The characteristic feature of these defects is a high specific surface distributed within the entire volume of the defect. This indicates an internal structure or complex shape, with subdefects at a scale below the camera pixel resolution. The other type is shown in the enlarged detail of Figure 15b for specimen 2: there are crescent-shaped structures in the image. These crescents are the refraction-enhanced edges of (rather circular) voids and, therefore, correspond to empty pores (i.e., with no internal structure). Note that only the top and bottom edges of the pores are enhanced due to the sensitivity to interface orientation of the SXRR measurement.

We could conclude that a low  $E_v$  would cause unmolten powder to be retained in discontinuities, while an excessive  $E_v$  would induce air bubbles.

## 5. Synchrotron X-Ray Refraction Computed Tomography

As mentioned in the introductory section of X-ray refraction, SXRR can be extended to a 3D investigation by simply rotating the specimen over 360°, acquiring refraction radiographs, and a 3D volume can be reconstructed by means of conventional algorithms (e.g.,).<sup>[60]</sup> This is called synchrotron X-ray refraction computed tomography (SXRCT). While SXCT allows 3D representations of density distribution inside specimens, SXRCT allows 3D representations of the specific internal surfaces. Both 3D techniques are, therefore, fully quantitative. The following examples show how SXRCT can quantify damage in materials, providing results that well complement those of SXCT. In contrast to the conventional SXCT, the SXRCT, like the SXRR, uses an analyzer crystal between the specimen and the detector (see Figure 9 left). However, for practical reasons (i.e., due to time constraints), it is not possible to sample a complete rocking curve (about 50 acquisitions) for each projection angle ( $\approx 1500$  angular positions) of a tomographic scan. Therefore, the analyzer crystal is adjusted to the (theoretical) maximum of its rocking curve (e.g. 3.779° at 30 keV) for the SXRCT measurement. At this setting, all X-rays, which are deflected by refraction events within the specimen, are rejected by the analyzer crystal causing an additional attenuation of the X-rays in the projections, on top of the attenuation described by the linear attenuation coefficient  $\mu$ . This effect is described by adding the refraction value  $C_m$  to the exponent of Lambert–Beer’s law of attenuation. The X-ray intensity  $I_R$  measured at the maximum of the rocking curve is, therefore, described by the following equation, where  $I_{R0}$  is the X-ray intensity at the maximum of the rocking curve without any specimen and  $t$  is the thickness of the specimen.

$$I_R = I_{R0} \cdot e^{-(\mu + C_m) \cdot t} \quad (3)$$

To determine the refraction value  $C_m$ , an absorption-based SXCT scan is performed (i.e., without the analyzer crystal). The projections in such scan yield the total transmitted X-ray intensity  $I_{trans}$ , which is determined by the linear attenuation coefficient  $\mu$  and the incident beam intensity  $I_{trans,0}$ .

$$I_{trans} = I_{trans,0} \cdot e^{-\mu \cdot t} \quad (4)$$

Using the series expansion of the logarithm, the refraction value  $C_m$  is then expressed as follows

$$C_m = \frac{1}{t} \cdot \left( 1 - \frac{I_R \cdot I_{trans,0}}{I_{R,0} \cdot I_{trans}} \right) \quad (5)$$

To reconstruct the 3D distribution of the refraction value  $C_m$ , projections representing the quantity  $C_m \cdot t$  are required. For this purpose, both CT scans—with and without analyzer crystal—are registered to each other and then processed together accordingly. Further information about the imaging technique can be found in other studies.<sup>[47a,49a,59]</sup> In the following, we report two eminent applications of SXRCT. In fact, the detectability of defects is limited to the spatial resolution in SXCT: the smallest detectable object corresponds to the smallest object that can be imaged. This is not the case for SXRCT, where detectability is enhanced by the refraction phenomenon.

### 5.1. 3D X-Ray Refraction Imaging of Damage in a Metal Matrix Composite after Low Cycle Fatigue

Fiber composites bridge the gap between demands on light weight and high strength of materials. It has been shown in the earlier sections that SXRR is extremely suited to characterize defects of all kinds in such materials. However, in common glass or carbon-reinforced plastics, the fiber diameter (typically 5–10  $\mu\text{m}$ ) is too small to image the fibers as individuals. In this study, we investigated MMC containing larger fibers.<sup>[44a]</sup> We used a cylindrically shaped (3.5 mm-diameter) low-cycle-fatigue (LCF) titanium matrix composite specimen provided by MTU Aero Engines, Germany. Reinforcing continuous fibers were SCS6 from Textron with a diameter of 140  $\mu\text{m}$  (33  $\mu\text{m}$  carbon fiber core enveloped by SiC). Composite samples were then prepared by hot isostatic pressing (HIP). Static and cyclic forces were applied in parallel to the fibers to obtain several mechanical parameters. After the tests the specimens were examined by metallographic methods and the fractured surfaces were analyzed.

In a conventional (i.e., absorption-based) radiograph (Figure 16a), the main fatigue crack is hardly recognizable and appears bright (due to lower absorption). It seems to extend over the left side of the sample, only. In the corresponding SXRR image (Figure 16b), the crack is highly contrasted and appears black (due missing, refracted beam portions). It extends through the entire sample diameter and shows side branches. To fully detect the defects in the MMC sample, SXRCT measurements were performed in two sample orientations. Figure 16c shows a 3D refraction tomographic reconstruction of the composite LCF specimen, acquired with the sample axis within the



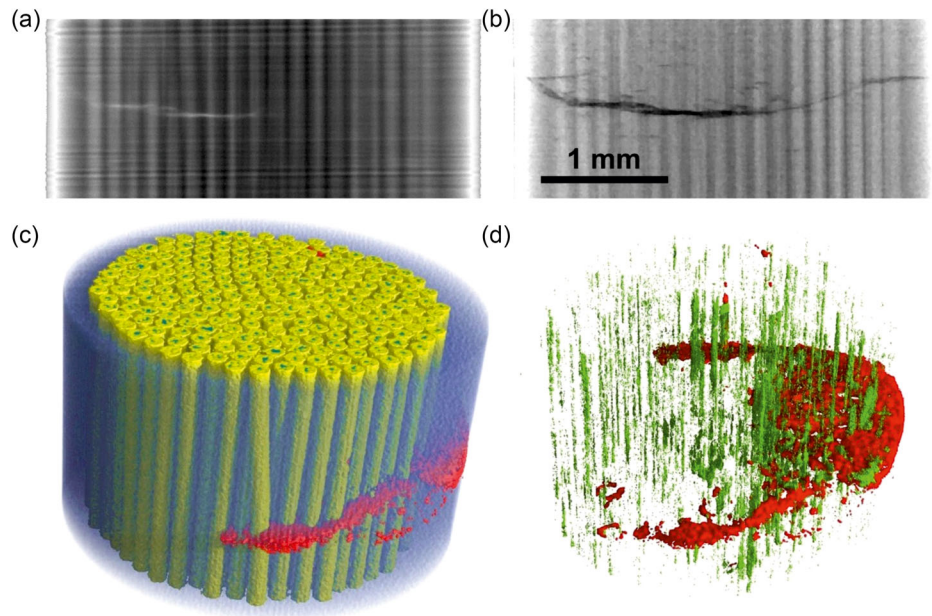


**Figure 16.** Radiographic contrast of conventional a) absorption versus b) SXRR. Note the extension of the horizontal fatigue crack. 3D SXRCT reconstruction of the MMC sample after LCF damaging. c) View through the semitransparent Ti matrix (blue) on solid SiC fibers (yellow) and fatigue cracks of the matrix (red) and d) the extracted damage surfaces of different types, fatigue cracks (red), and fiber debonding (green). Note that the different types of damages were obtained from two SXRCT measurements in different sample orientations. Reproduced with permission.<sup>[44a]</sup> Copyright 2009, Wiley-VCH.

scattering plane. As in the case of transmission CT measurements (not shown here), the visualization contains all information about the fiber distribution and orientation in the Ti matrix. The fatigue-induced macrocrack is clearly visible (red color). By acquiring refraction projections with the sample mounted horizontally, we are sensitive to axial defects and can separately extract fiber debonding (depicted in green in Figure 16d). Debonded fibers generate a higher refraction signal since the number of interfaces is increased (matrix/air and air/fiber instead of matrix/fiber). Both damage surfaces are shown together in Figure 16d. The fatigue cracks of the Ti matrix are oriented perpendicular to the load direction and located in the Ti matrix. Fiber debonding is oriented parallel to the load direction. The two different types of flaws are expected to selectively explain the material's sensitivity to different kinds of loads.

## 5.2. Imaging of Hydrogen-Assisted Cracking in Duplex Stainless Using Refraction-Enhanced Synchrotron CT

The demands placed on steels, particularly in the field of aggressive environments, have risen steadily in recent decades. Both economic and design aspects are leading to ever higher requirements in terms of resistance to corrosive media and materials strength. Despite the outstanding mechanical and corrosion properties, cases of damage associated with the negative effects of hydrogen have occurred in many industrial sectors. These mostly take place in the form of degradation of the mechanical properties by hydrogen embrittlement (HE). Furthermore, this damage can lead to hydrogen-assisted cracking (HAC) at a given critical combination of microstructure, strain, and hydrogen concentration.

In ref. [61], we showed a quantitative characterization of damage caused by HAC in a 2101 lean duplex stainless steels (DSS).

The detection of individual cracks is still a major challenge, since it needs high-resolution (imaging) methods (the grain size of the phases in DSS is of the order of 10  $\mu\text{m}$ ); at the same time, a sound statistical analysis requires a large number of defects to be detected (and eventually imaged) and, therefore, a large FoV. 3D tomographic reconstructions were used to determine the size and location of the cracks in hydrogen-charged tensile specimens subjected to different load levels (plastically deformed and fully fractured). **Figure 17** shows the reconstruction of the SXRCT data sets of three specimens (virgin, uncharged (A), H<sub>2</sub>-charged and plastically deformed (B), H<sub>2</sub>-charged and ruptured (C)) and the segmentation of the defects therein. It shows that cracks occur predominantly at the outer edges of all the specimens and that both the number and the size of these cracks increase with increasing mechanical load (specimens C versus B) and increasing hydrogen content (specimens B and C versus A). Comparison among specimens shows that the cracks at the outer surface of the specimen grow with increasing load, while the defects closer to the center remain largely unaffected by the increase of load. In the volumes reconstructed with SXRCT, 159 defects were found for sample B and 602 for sample C, while only 74 and 373 defects were found in the volumes reconstructed with SXCT, respectively. In fact, the detectability of defects with SXCT is limited to its spatial resolution. This is not the case with SXRCT, where detectability is enhanced by the phenomenon of refraction. In this case study, due to the better contrast of the SXRCT images compared to the SXCT images, more individual defects could also be imaged (at the same spatial resolution). We could conclude that the charging process already induces damage, but such damage remains close to the surface, while severe plastic deformation induces crack propagation (toward the interior of the specimen).

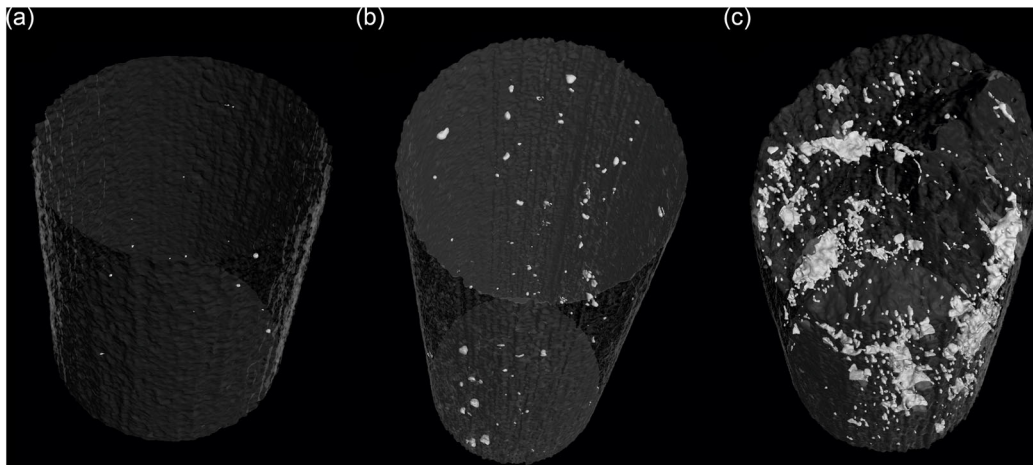


**Figure 17.** 3D rendering of cracks in specimens A (uncharged), B (74 ppm H<sub>2</sub> charged and plastically deformed), and C (74 ppm H<sub>2</sub> charged and completely fractured) obtained from the reconstructed volume (outer diameter of the specimen 1.3 mm) of refraction values  $C_m$ . Reproduced with permission.<sup>[61]</sup> Copyright 2022, Wiley-VCH.

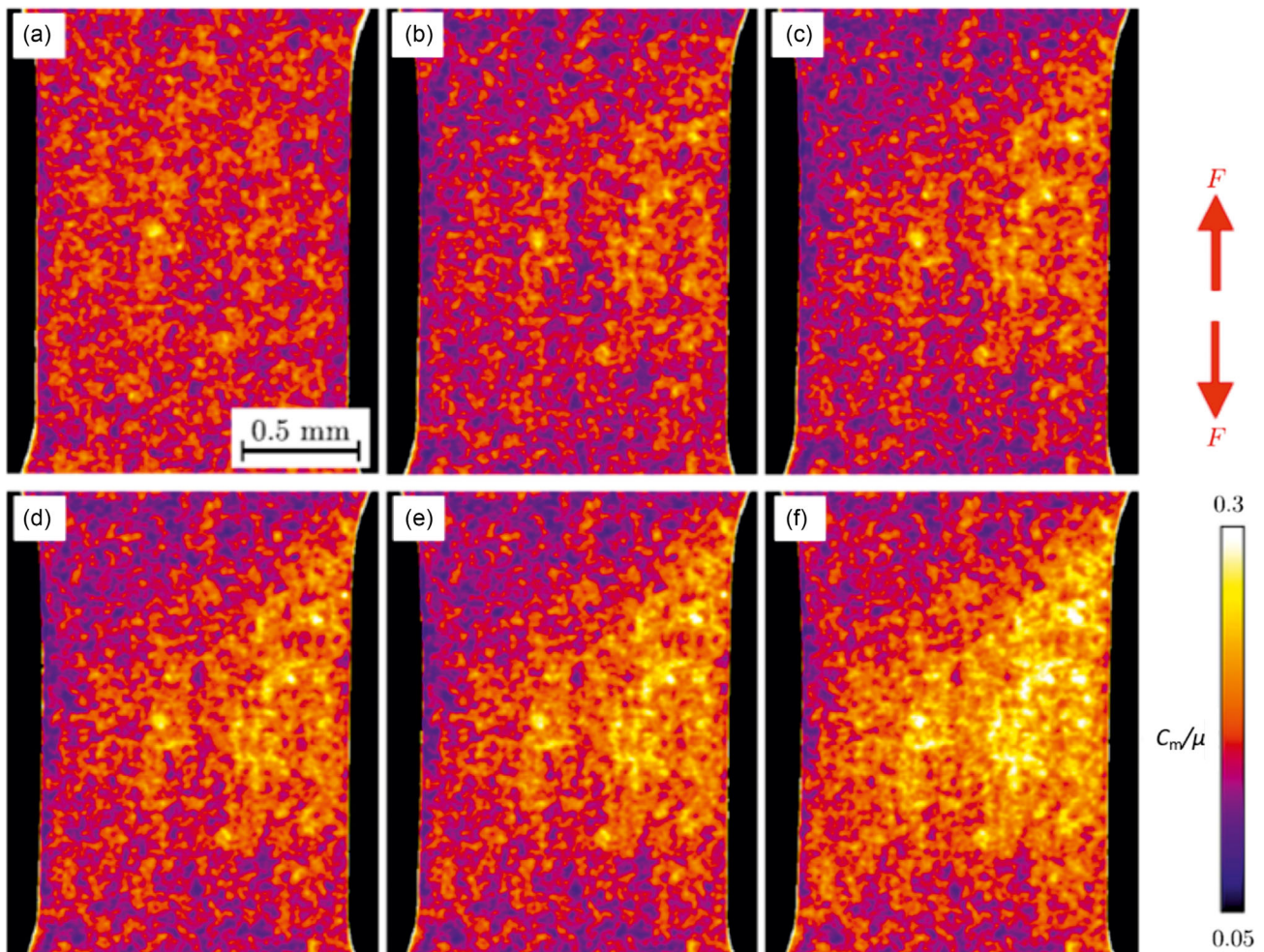


**Figure 18.** Color-coded distribution of the relative specific surface  $C_m/\mu$  in an Al/Al<sub>2</sub>O<sub>3</sub> MMC obtained from SXRR for applied stress  $\sigma$  of a) 11 MPa, b) 294 MPa, c) 319 MPa, d) 323 MPa, e) 328 MPa, and f) 331 MPa. High values of the specific surface indicate high amount of damage. Reproduced with permission.<sup>[47a]</sup> Copyright 2018, Springer.

## 6. In Situ and Operando Experiments

### 6.1. Damage Evolution in an Al/Al<sub>2</sub>O<sub>3</sub> MMC under Uniaxial Tension

Due to their low density, high strength, and high stiffness, aluminum alloy-based MMCs are valuable structural materials, for example, in automotive and aviation applications. These composite materials usually possess poor fracture properties, which limit

their industrial utilization. Therefore, much attention has been paid to mechanical load-induced damage mechanisms in MMCs. In the case of particle-reinforced MMCs, these mechanisms are generally divided into three classes: 1) matrix ductile failure; 2) matrix/particle decohesion; and 3) particle cracking. In the study we report here,<sup>[47a]</sup> SXRR was successfully used the first time to monitor the mechanically induced (external tensile stress) damage evolution in an Al6061 matrix alloy, reinforced with 10% ceramic Al<sub>2</sub>O<sub>3</sub> particles. This approach allowed to gather

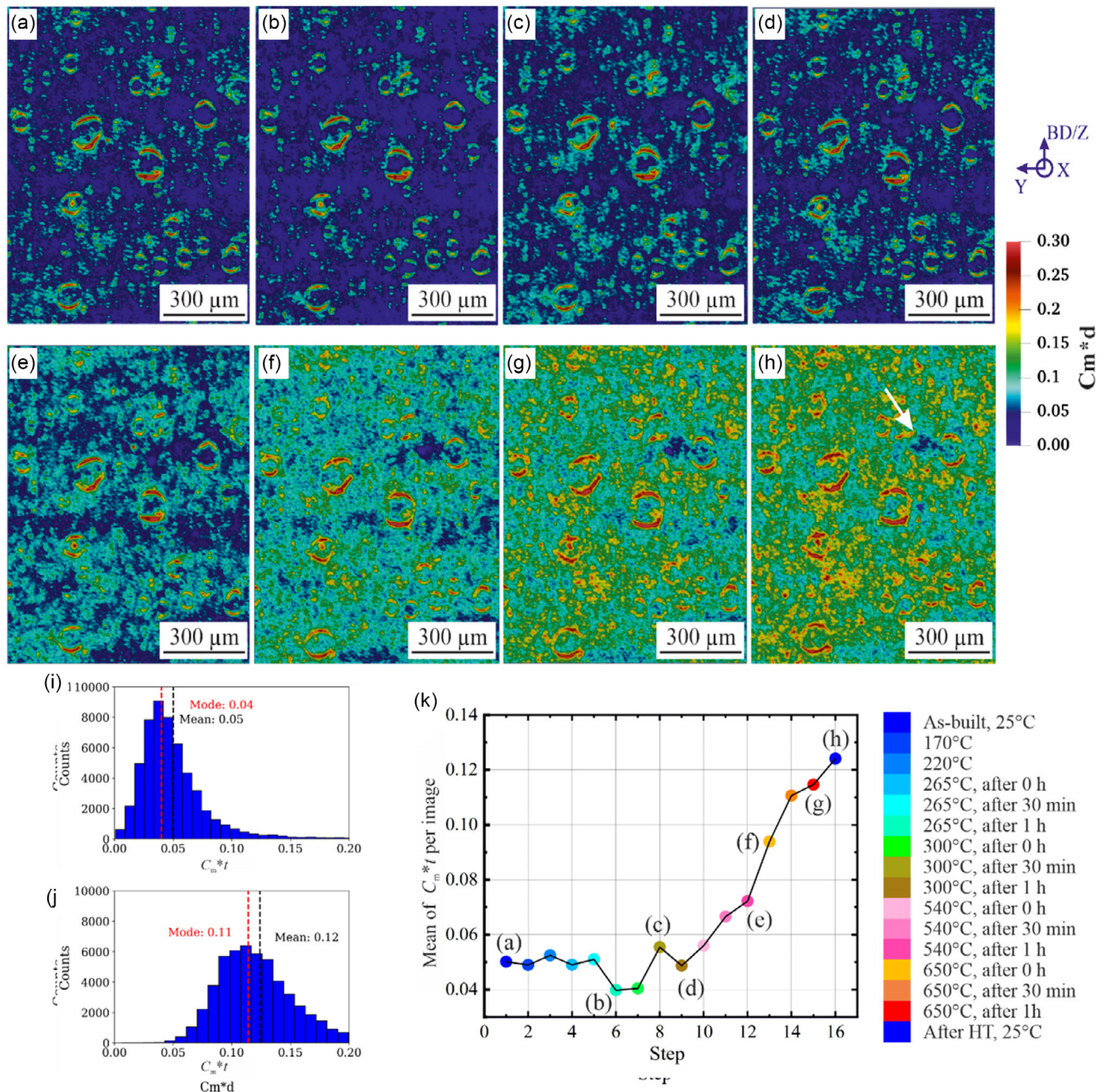


**Figure 19.** Color-coded  $C_m \cdot t$  refraction images recorded at a) room temperature (25 °C), b) 265 °C after 1 h, c) 300 °C after 30 min, d) 300 °C after 1 h, e) 540 °C after 1 h, f) 650 °C after 0 h, g) 650 °C after 1 h, and h) room temperature after heat treatment. Histograms of the  $C_m \cdot t$  values of the image recorded at i) 25 °C (as-built (a)) and j) 25 °C (After HT (h)). k) Plot of the mean of  $C_m \cdot t$  per image against the temperature steps. Reproduced with permission.<sup>[62]</sup> Copyright 2022, Elsevier.

nanometric information about void nucleation and damage evolution on the macroscale in situ during quasistatic loading. **Figure 18** shows the development of the relative specific surface area  $C_m/\mu$  (damage) during a tensile test, exemplified at six load states  $\sigma$  (see figure caption). In the initial state (a), the elevated  $C_m/\mu$  is caused by the interfaces between the Al matrix and the  $Al_2O_3$  particles as well as at the surface of initial imperfections (cracks, pores, and debonded particles). At the first stress level, the relative specific surface decreases on the left-hand side of the specimen and starts increasing on the right side due to a superimposed bending moment during the tensile test, which led to the left-hand side of the sample being under compression. Therefore, initial cracks and cavities tended to close and the specific surface was reduced. As the tensile test progressed,  $C_m/\mu$  increased due to the formation and growth of defects. In conventional absorption-based imaging, no indication of damaging in the sample up to the last load stage became apparent (shown in Figure 8 in ref. [47a]). This documents the superior detectability of SXRR as compared to absorption-based radiography and proves that the defects observed with SXRR are smaller than the actual spatial resolution. In Figure 18, it is apparent that severe

damage occurs when the specimen approaches rupture; the region where the rupture would occur is clearly indicated by the SXRR signal increase. Therefore, SXRR could be successfully used to predict the location of catastrophic failure in such composites.

## 6.2. Microstructure and Porosity Evolution as a Function of Temperature

As a further method development, SXRR was recently combined with in situ heat treatment to monitor microstructure and porosity evolution as a function of temperature in a L-PBF-manufactured AlSi10Mg alloy, where the initial eutectic Si network is known to disintegrate and spheroidize into larger particles with increasing temperature.<sup>[62]</sup> Such alloy is also prone to thermally induced porosity (TIP). By means of SXRR, the changes in the Si phase morphology upon heating (currently only possible using scanning electron microscopy) and the growth of pores (usually studied via XCT, but on much smaller FoV) could be observed. The results show the great

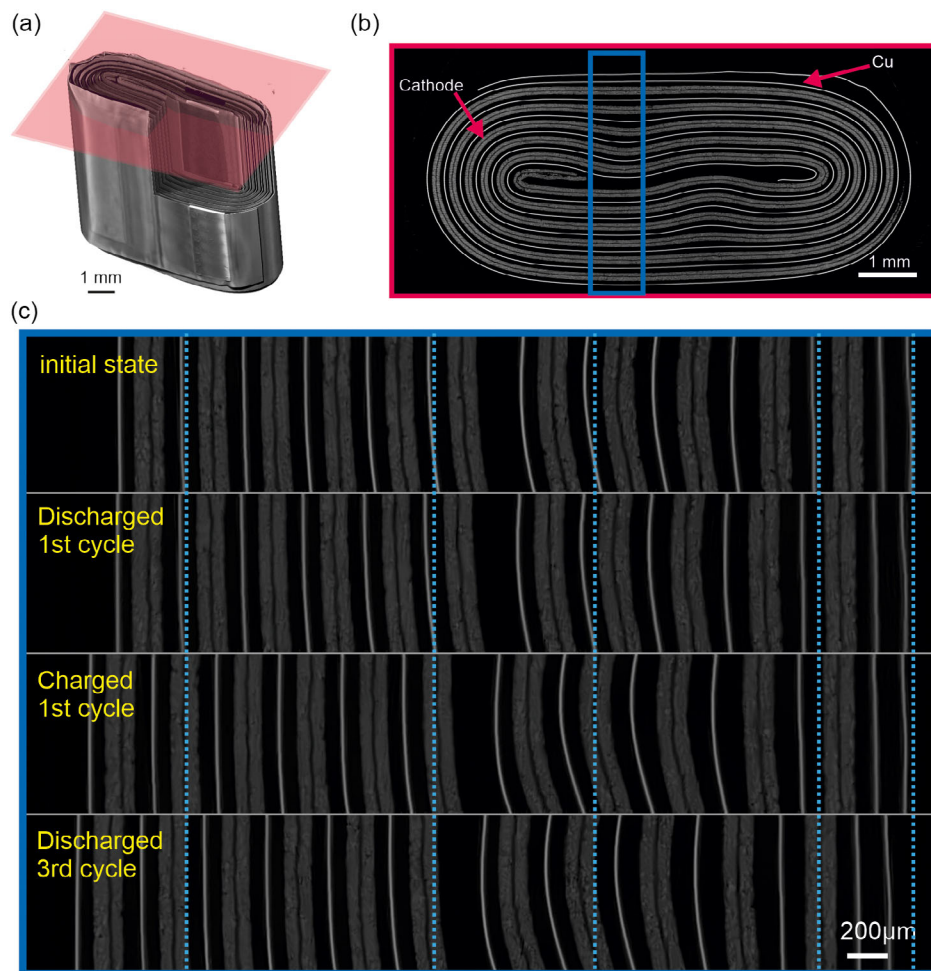


**Figure 20.** Operando investigation of the cycling effect on lithium-ion batteries. a) 3D representation of a pouch lithium-ion cell. b) Electrode jellyroll assembly. c) Temporal evolution of the selected jellyroll section at different stages of the cycling experiment. Blue guiding lines mark positions of selected Cu current collectors at each stage.

potential of in situ SXRR as a tool to gain in-depth knowledge of the susceptibility of any material to thermally induced damage and/or microstructure evolution over statistically relevant volumes.

Figure 19 shows the evolution of  $C_m \cdot t$  maps as a function of temperature. The porosity mainly consists of large spherical pores yielding crescent-shaped features, for which the  $C_m \cdot t$  values vary from about 0.08 to 0.28 in the initial conditions (Figure 19a) and from 0.17 to 0.3 in the final temperature step (Figure 19h). The increase of  $C_m \cdot t$  values of the background (i.e., from 0.05 to 0.15) is generated by the increase of smaller gas pores (induced by both pore growth and nucleation). Also note that the increase of  $C_m \cdot t$  is spatially heterogeneous throughout the entire heat treatment cycle (Figure 19a–h), and the final stage indicates that some regions remain at the original 0.04–0.05  $C_m \cdot t$  values throughout the entire heating cycle (an example is indicated with a white arrow in Figure 19h).

### 6.3. Operando SXCT studies on Li-Ion Batteries

A commercially available lithium-ion cell in pouch format (see Figure 20a) was examined in operando using SXCT while being charged and discharged at various C rates (current/capacity). For optimal imaging, the smallest available cell (7 mm × 7 mm × 4 mm) was chosen having a capacity of 30 mAh. The DMM provided a monochromatic beam with 42 keV, a FoV of 9.2 mm × 1.5 mm, and a pixel size of 3.6 μm (Figure 20b,c). XCT was conducted continuously with each tomographic scan using around 2000 projections. This took 1 h to complete, while the lithium-ion battery was first discharged from the initial state at a current rate of C/2 (1C => 30 mA), followed by two more charging–discharging cycles using 1C charging rate as well as 2C and 4C discharging rates, respectively.

The battery is built of spirally twisted electrode layers also known as jellyroll electrode assembly. Copper current collectors covered by graphite anode material as well as lithium metal oxide cathodes on aluminum current collectors are shown in Figure 20b. A small portion of the jellyroll is selected to study effects of cycling on the electrodes.

The battery is fixed at the right-hand side on the sample holder. However, expansion is obvious after the first charging cycle is finished. Since the casing of the pouch cell is not a rigid body, gas evolution easily changes the cell shape. Therefore, more movement is observed when the cell is cycled with higher C rates. A nonuniform distance of the electrodes can be observed. This indicates that the electrodes partially delaminate, which hints to larger internal resistances compared to well-compressed battery assemblies.

## 7. Summary and Outlook

The imaging conducted at BAMline has run very successfully since the beamline was commissioned and serves a user community from a wide range of research fields. This is demonstrated by numerous publications. Especially, refraction-enhanced imaging for submicrometer features as well as an element sensitive technique increase the range of imaging options at the beamline.

Within the last two years, the beamline is being strongly upgraded for both, hardware and software. The main improvements regard the photon flux, thanks to an upgraded DMM as well as the capability to record tomographies, much faster thanks to an upgraded detector system.<sup>[9]</sup> Thanks to the higher time resolution, the possible applications move more toward operando and in situ studies, thus allowing more tensile or compressive states and more temperature steps to be scanned or visualizing true dynamics while fast charging of batteries, for example. This implies of course the development of corresponding techniques and sample environment, optimized for X-ray imaging.

## Acknowledgements

The authors like to thank Wolf Görner, initiator and driving force behind the realization of BAMline, as well as Ralf Britzke, Michael Sintschuk, and Thomas Wolk for beamline support and the Helmholtz-Zentrum Berlin for the allocation of beamtime.

Open Access funding enabled and organized by Projekt DEAL.

## Conflict of Interest

The authors declare no conflict of interest.

## Keywords

material science, radiography, refraction, tomography, X-ray imaging

Received: July 18, 2022

Revised: December 21, 2022

Published online:

- [1] W. Görner, M. P. Hentschel, B. R. Müller, H. Riesemeier, M. Krumrey, G. Ulm, W. Diete, U. Klein, R. Frahm, *Nucl. Instrum. Methods Phys. Res., Sect. A* **2001**, 467–468, 703.
- [2] a) H. Riesemeier, K. Ecker, W. Görner, B. R. Müller, M. Radtke, M. Krumrey, *X-Ray Spectrom.* **2005**, 34, 160; b) A. G. Buzanich, M. Radtke, U. Reinholz, H. Riesemeier, F. Emmerling, *J. Synchrotron Radiat.* **2016**, 23, 769.
- [3] A. Rack, S. Zabler, B. R. Müller, H. Riesemeier, G. Weidemann, A. Lange, J. Goebbels, M. Hentschel, W. Görner, *Nucl. Instrum. Methods Phys. Res., Sect. A* **2008**, 586, 327.
- [4] B. R. Müller, A. Lange, M. Harwardt, M. P. Hentschel, *Highlights/BESSY, Vol. 2003*, Bessy, Berlin **2004**, p. 321.
- [5] T. M. Buzug, *Computed Tomography*, Springer-Verlag Berlin, Berlin **2011**.
- [6] L. A. Feldkamp, L. C. Davis, *IEEE Trans. Med. Imaging* **1988**, 7, 73.
- [7] a) A. H. Andersen, *IEEE Trans. Med. Imaging* **1989**, 8, 50; b) G. T. Herman, A. Lent, S. W. Rowland, *J. Theor. Biol.* **1973**, 42, 1.
- [8] M. P. Hentschel, A. Lange, J. Schors, in *presented at 3rd Conf. on Testing, Reliability, and Application of Micro and Nano-Material Systems*, San Diego, CA, March **2005**.
- [9] H. Markötter, M. Sintschuk, R. Britzke, S. Dayani, G. Bruno, *J. Synchrotron Radiat.* **2022**, 29, 1292.
- [10] a) C. Vercootere, S. Maury, *Anthropologie* **2018**, 122, 402; b) I. Reiche, K. Mueller, A. Staude, J. Goebbels, H. Riesemeier, *J. Anal. At. Spectrom.* **2011**, 26, 1802.
- [11] H. P. Reike, A. Bukejs, T. Arlt, N. Kardjilov, I. Manke, *Zootaxa* **2017**, 4242, 578.

- [12] T. Arlt, F. Wieder, I. Ritsche, A. Hilger, N. Kardjilov, J. M. Fahlke, O. Hampe, I. Manke, *Mater. Test.* **2018**, *60*, 173.
- [13] P. Zaslansky, S. Zabler, P. Fratzl, *Dent. Mater.* **2010**, *26*, E1.
- [14] R. Zehbe, H. Riesemeier, C. J. Kirkpatrick, C. Brochhausen, *Micron* **2012**, *43*, 1060.
- [15] a) A. Isaac, R. Conti, C. M. Viana, F. I. Sket, L. A. Montoro, A. Hilger, I. Manke, *Ind. Crops Prod.* **2016**, *86*, 289; b) A. Isaac, F. A. F. Antunes, R. Conti, L. A. Montoro, A. Malachias, P. Massara, G. Kitten, H. Markötter, I. Manke, S. S. da Silva, *Ind. Crops Prod.* **2018**, *114*, 19.
- [16] S. Evsevlev, T. Mishurova, S. Cabeza, R. Koos, I. Sevostianov, G. Garces, G. Requena, R. Fernandez, G. Bruno, *Mater. Sci. Eng., A* **2018**, *736*, 453.
- [17] a) A. Lange, M. P. Hentschel, A. Kupsch, *Mater. Test.* **2008**, *50*, 272; b) A. Kupsch, A. Lange, M. P. Hentschel, B. R. Müller, *Mater. Test.* **2010**, *52*, 394; c) A. Kupsch, A. Lange, M. P. Hentschel, S. Lück, V. Schmidt, R. Grothausmann, A. Hilger, I. Manke, *J. Microsc.* **2016**, *267*, 36.
- [18] a) S. Magkos, A. Kupsch, G. Bruno, *Rev. Sci. Instrum.* **2020**, *91*, 103107; b) S. Magkos, A. Kupsch, G. Bruno, *J. Imaging* **2021**, *7*, 147.
- [19] I. Manke, H. Markötter, C. Tötze, N. Kardjilov, R. Grothausmann, M. Dawson, C. Hartnig, S. Haas, D. Thomas, A. Hoell, C. Genzel, J. Banhart, *Adv. Eng. Mater.* **2011**, *13*, 712.
- [20] a) P. Krüger, H. Markötter, M. Klages, J. Haussmann, T. Arlt, H. Riesemeier, C. Hartnig, J. Banhart, I. Manke, J. Scholta, *Mater. Test.* **2010**, *52*, 712; b) P. Krüger, H. Markötter, J. Haussmann, M. Klages, T. Arlt, J. Banhart, C. Hartnig, I. Manke, J. Scholta, *J. Power Sources* **2011**, *196*, 5250; c) J. Haußmann, H. Markötter, R. Alink, A. Bauder, K. Dittmann, I. Manke, J. Scholta, *J. Power Sources* **2013**, *239*, 611; d) H. Markötter, I. Manke, J. Haußmann, T. Arlt, M. Klages, P. Krüger, C. Hartnig, J. Scholta, B. R. Müller, H. Riesemeier, J. Banhart, *Micro Nano Lett.* **2012**, *7*, 689; e) H. Markötter, J. Haußmann, R. Alink, C. Tötze, T. Arlt, M. Klages, H. Riesemeier, J. Scholta, D. Gerteisen, J. Banhart, I. Manke, *Electrochem. Commun.* **2013**, *34*, 22; f) T. Arlt, I. Manke, K. Wippermann, H. Riesemeier, J. Mergel, J. Banhart, *J. Power Sources* **2013**, *221*, 210; g) T. Arlt, M. Klages, M. Messerschmidt, H. Riesemeier, J. Scholta, J. Banhart, I. Manke, *ECS Electrochem. Lett.* **2014**, *3*, F7; h) C. Tötze, G. Gaiselmann, M. Osenberg, J. Bohner, T. Arlt, H. Markötter, A. Hilger, F. Wieder, A. Kupsch, B. R. Müller, M. P. Hentschel, J. Banhart, V. Schmidt, W. Lehnert, I. Manke, *J. Power Sources* **2014**, *253*, 123.
- [21] a) K. Seidenberger, F. Wilhelm, J. Haußmann, H. Markötter, I. Manke, J. Scholta, *J. Power Sources* **2013**, *239*, 628; b) G. Gaiselmann, C. Tötze, I. Manke, W. Lehnert, V. Schmidt, *J. Power Sources* **2014**, *257*, 52; c) C. Tötze, I. Manke, G. Gaiselmann, J. Bohner, B. R. Müller, A. Kupsch, M. P. Hentschel, V. Schmidt, J. Banhart, W. Lehnert, *Rev. Sci. Instrum.* **2015**, *86*, 043702; d) M. Fazeli, J. Hinebaugh, Z. Fishman, C. Tötze, W. Lehnert, I. Manke, A. Bazylak, *J. Power Sources* **2016**, *335*, 162; e) U. U. Ince, H. Markötter, M. G. George, H. Liu, N. Ge, J. Lee, S. S. Alrwashdeh, R. Zeis, M. Messerschmidt, J. Scholta, A. Bazylak, I. Manke, *Int. J. Hydrogen Energy* **2018**, *43*, 391.
- [22] a) W. Maier, T. Arlt, C. Wannek, I. Manke, H. Riesemeier, P. Krüger, J. Scholta, W. Lehnert, J. Banhart, D. Stolten, *Electrochem. Commun.* **2010**, *12*, 1436; b) T. Arlt, W. Maier, C. Tötze, C. Wannek, H. Markötter, F. Wieder, J. Banhart, W. Lehnert, I. Manke, *J. Power Sources* **2014**, *246*, 290.
- [23] a) A. Schröder, K. Wippermann, T. Arlt, T. Sanders, T. Baumhofer, H. Markötter, J. Mergel, W. Lehnert, D. Stolten, I. Manke, J. Banhart, *Fuel Cells* **2013**, *13*, 371; b) T. Arlt, A. Schröder, K. Heyne, H. Riesemeier, K. Wippermann, W. Lehnert, I. Manke, *J. Power Sources* **2015**, *297*, 83.
- [24] S. Risse, A. Juhl, S. Mascotto, T. Arlt, H. Markötter, A. Hilger, I. Manke, M. Fröba, *J. Phys. Chem. Lett.* **2020**, *11*, 5674.
- [25] T. Mitsch, Y. Krämer, J. Feinauer, G. Gaiselmann, H. Markötter, I. Manke, A. Hintennach, V. Schmidt, *Materials* **2014**, *7*, 4455.
- [26] D. Schröder, C. L. Bender, T. Arlt, M. Osenberg, A. Hilger, S. Risse, M. Ballauff, I. Manke, J. Janek, *J. Phys. D: Appl. Phys.* **2016**, *49*, 12.
- [27] a) F. Sun, H. Markötter, D. Zhou, S. S. S. Alrwashdeh, A. Hilger, N. Kardjilov, I. Manke, J. Banhart, *ChemSusChem* **2016**, *9*, 946; b) F. Sun, L. Zielke, H. Markoetter, A. Hilger, D. Zhou, R. Moroni, R. Zengerle, S. Thiele, J. Banhart, I. Manke, *ACS Nano* **2016**, *10*, 7990.
- [28] T. Thiede, T. Mishurova, S. Evsevlev, I. Serrano-Munoz, C. Gollwitzer, G. Bruno, *Quantum Beam Sci.* **2019**, *3*, 12.
- [29] T. W. Ridler, S. Calvard, *IEEE Trans. Syst. Man Cybern.* **1978**, *8*, 630.
- [30] J. Schindelin, I. Arganda-Carreras, E. Frise, V. Kaynig, M. Longair, T. Pietzsch, S. Preibisch, C. Rueden, S. Saalfeld, B. Schmid, J. Y. Tinevez, D. J. White, V. Hartenstein, K. Eliceiri, P. Tomancak, A. Cardona, *Nat. Methods* **2012**, *9*, 676.
- [31] S. Evsevlev, S. Cabeza, T. Mishurova, G. Garcés, I. Sevostianov, G. Requena, M. Boin, M. Hofmann, G. Bruno, *J. Mater. Sci.* **2020**, *55*, 1049.
- [32] S. Evsevlev, I. Sevostianov, T. Mishurova, M. Hofmann, G. Garces, G. Bruno, *Metall. Mater. Trans. A* **2020**, *51*, 3104.
- [33] S.-N. Zhao, X.-Z. Song, S.-Y. Song, H.-J. Zhang, *Coord. Chem. Rev.* **2017**, *337*, 80.
- [34] H. Thakkar, S. Eastman, Q. Al-Naddaf, A. A. Rowanghi, F. Rezaei, *ACS Appl. Mater. Interfaces* **2017**, *9*, 35908.
- [35] P. Scholz, A. Ulbricht, Y. Joshi, C. Gollwitzer, S. M. Weidner, *Int. J. Mater. Res.* **2020**, *111*, 55.
- [36] a) X. E. Gros, in *Applications of NDT Data Fusion*, Springer, New York, NY **2001**; b) M.-A. Ploix, V. Garnier, D. Breysse, J. Moysan, *NDT & E Int.* **2011**, *44*, 442.
- [37] F. Pedregosa, G. Varoquaux, A. Gramfort, V. Michel, B. Thirion, O. Grisel, M. Blondel, P. Prettenhofer, R. Weiss, V. Dubourg, J. Vanderplas, A. Passos, D. Cournapeau, M. Brucher, M. Perrot, E. Duchesnay, *J. Mach. Learn. Res.* **2011**, *12*, 2825.
- [38] T. Arlt, I. Manke, K. Wippermann, C. Tötze, H. Markötter, H. Riesemeier, J. Mergel, J. Banhart, *Electrochem. Commun.* **2011**, *13*, 826.
- [39] D. R. Lammel, T. Arlt, I. Manke, M. C. Rillig, *Front. Environ. Sci.* **2019**, *7*.
- [40] S. Evsevlev, B. R. Müller, A. Lange, A. Kupsch, *Nucl. Instrum. Methods Phys. Res., Sect. A* **2019**, *916*, 275.
- [41] A. Larsson, M. Siegbahn, I. Waller, *Naturwissenschaften* **1924**, *12*, 1212.
- [42] M. P. Hentschel, R. Hosemann, A. Lange, B. Uther, R. Brückner, *Acta Crystallogr., Sect. A: Found. Crystallogr.* **1987**, *43*, 506.
- [43] A. Kupsch, B. R. Müller, A. Lange, G. Bruno, *J. Eur. Ceram. Soc.* **2017**, *37*, 1879.
- [44] a) B. R. Müller, A. Lange, M. Harwardt, M. P. Hentschel, *Adv. Eng. Mater.* **2009**, *11*, 435; b) W. Görner, M. P. Hentschel, B. R. Müller, H. Riesemeier, M. Krumrey, G. Ulm, W. Dietsch, U. Klein, R. Frahm, *Nucl. Instrum. Methods Phys. Res., Sect. A* **2001**, *467*, 703.
- [45] D. Mani, A. Kupsch, B. R. Müller, G. Bruno, *J. Imaging* **2022**, *8*, 206.
- [46] C. A. Schneider, W. S. Rasband, K. W. Eliceiri, *Nat. Methods* **2012**, *9*, 671.
- [47] a) J. Nellesen, R. Laquai, B. R. Müller, A. Kupsch, M. P. Hentschel, N. B. Anar, E. Soppa, W. Tillmann, G. Bruno, *J. Mater. Sci.* **2018**, *53*, 6021; b) S. Cabeza, B. R. Müller, R. Pereyra, R. Fernandez, G. Gonzalez-Doncel, G. Bruno, *J. Appl. Crystallogr.* **2018**, *51*, 420.
- [48] R. Laquai, B. Müller, G. Kasperovich, G. Requena, J. Haubrich, G. Bruno, *Mater. Perform. Charact.* **2020**, *9*, 82.
- [49] a) S. Cabeza, B. R. Müller, R. Pereyra, R. Fernandez, G. Gonzalez-Doncel, G. Bruno, *J. Appl. Crystallogr.* **2018**, *51*, 420; b) A. Kupsch,

- V. Trappe, B. R. Müller, G. Bruno, *IOP Conf. Ser.: Mater. Sci. Eng.* **2020**, *942*, 012035.
- [50] R. C. Cooper, G. Bruno, M. R. Wheeler, A. Pandey, T. R. Watkins, A. Shyam, *Acta Mater.* **2017**, *135*, 361.
- [51] G. A. P. P. Merkel, NY, US), T. Tao (Big Flats, NY, US) (G. A. Merkel, T. Tao) United States **2004**.
- [52] a) M. J. Readey, L. D. Rontanini, USA, **1990**; b) N. Saito, S. Y. Nishimura, M. Kawano, S. I. Araki, S. Sukenaga, K. Nakashima, T. Yasukouchi, *J. Am. Ceram. Soc.* **2010**, *93*, 2257.
- [53] G. Bruno, A. M. Efremov, B. Clausen, A. M. Balagurov, V. N. Simkin, B. R. Wheaton, J. E. Webb, D. W. Brown, *Acta Mater.* **2010**, *58*, 1994.
- [54] A. Kupsch, A. Lange, M. P. Hentschel, Y. Onel, T. Wolk, A. Staude, K. Ehrig, B. R. Müller, G. Bruno, *J. Ceram. Sci. Technol.* **2013**, *4*, 169.
- [55] C. Chen, B. R. Müller, O. I. Lebedev, F. Giovannelli, G. Bruno, F. Delorme, *Mater. Charact.* **2019**, *149*, 111.
- [56] R. Laquai, F. Gouraud, B. R. Müller, M. Huger, T. Chotard, G. Antou, G. Bruno, *Materials* **2019**, *12*, 1017.
- [57] B. R. Müller, R. C. Cooper, A. Lange, A. Kupsch, M. Wheeler, M. P. Hentschel, A. Staude, A. Pandey, A. Shyam, G. Bruno, *Acta Mater.* **2018**, *144*, 627.
- [58] A. P. Soares, D. Baum, B. Hesse, A. Kupsch, B. R. Müller, P. Zaslansky, *Dent. Mater.* **2021**, *37*, 201.
- [59] R. Laquai, B. R. Müller, G. Kasperovich, J. Haubrich, G. Requena, G. Bruno, *Mater. Res. Lett.* **2018**, *6*, 130.
- [60] L. A. Feldkamp, L. C. Davis, J. W. Kress, *J. Opt. Soc. Am. A* **1984**, *1*, 612.
- [61] R. Laquai, T. Schaupp, A. Griesche, B. R. Müller, A. Kupsch, A. Hannemann, T. Kannengiesser, G. Bruno, *Adv. Eng. Mater.* **2022**, *24*, 2101287.
- [62] I. Serrano-Munoz, I. Roveda, A. Kupsch, B. R. Müller, G. Bruno, *Mater. Sci. Eng., A* **2022**, *838*, 142732.
- [63] H. Markötter, I. Manke, P. Krüger, T. Arlt, J. Haussmann, M. Klages, H. Riesemeier, C. Hartnig, J. Scholta, J. Banhart, *Electrochem. Commun.* **2011**, *13*, 1001.



**Henning Markötter** studied physics at the Technical University Berlin, Germany, and worked there on a holographic data storage system. In 2010, he joined the “Imaging Group” at HZB and did a Ph.D. until 2013, in which he was working in the field of water transport processes in PEM fuel cell materials by means of synchrotron and neutron imaging. Now he is at the Federal Institute of Materials Research and Testing in the division “Micro Nondestructive Testing” as a beamline scientist of BAMline at the electron storage ring Bessy II responsible for CT activities.



**Bernd R. Müller** studied physics at Technische Universität Berlin where he presented his thesis in atomic physics in 1990. After several years in basic research at several European Synchrotron Facilities, he joined the X-ray topography group at BAM in 1995. At the Berlin Synchrotron Laboratory BESSY, he designed and completed the BAM beamline. His activities focus on the development and application of new techniques in high-energy synchrotron topography and computed tomography. He is a lecturer for X-ray imaging techniques in materials science at Technische Universität Berlin. In 2015, he received the Science Award of the DGZfP.